ANALYSIS OF FOUNTAIN EFFECT FOR TILTROTOR CONFIGURATION USING COMPUTATIONAL FLUID SIMULATION AND EXPERIMENTAL METHOD

BY

JE WON HONG

THESIS

Submitted in partial fulfillment of the requirements
for the degree of Master of Science in Aerospace Engineering
in the Graduate College of the
University of Illinois at Urbana-Champaign, 2017

Urbana, Illinois

Advisor:

Professor Phillip J. Ansell

Abstract

The study involves a tiltrotor's wing/rotor configuration design to properly test the model in both hover flight condition and crosswind condition replicated in the wind tunnel. To record data, a subsonic wind tunnel was utilized to test the wing/rotor configuration in different conditions of freestream velocity of V_∞ =10, 15, and 20 m/s, the blade pitch angle of θ =5°, 10°, and 15°, and across a range of crosswind angles of β = 0°-90°. Post-processing of the obtained data was performed to interpret flow interactions between the rotor and wing in crosswind flight conditions and influences on the fountain effect. Further, a CFD simulation tool was used for comparison to these experiments. Also, a PIV experiment was performed to visualize the fountain effect's flow structure, which occurred on the wing in the hover flight condition.

A series of wind tunnel tests performed indicated that lift coefficients of the wind tunnel tests and CFD results closely replicate each other's results for crosswind angles lower than 60°. Therefore, it can be stated that the URANS-based CFD methodology can simulate the tiltrotor's wing/rotor configuration performance for flight conditions of lower crosswind angles, ideally from 0° to 45° for this particular study.

Performing flow visualizations for crosswind flight conditions of lower crosswind angles indicated that the fountain effect is present in the hover flight condition. Then, the effect diminishes in the freestream flight condition. No significant change for thrust coefficient occurs. An induced flow beneath the rotor on the downstream side was observed to occur. Consequently, the thrust coefficient drops, indicating a performance decrease in higher crosswind angles.

To my beloved wife and best friend Haeley

Acknowledgement

This research was inspired from my internship at Aeromechanics branch at NASA Ames Research Center during the summer of 2015 under NASA International Internship (I^2) program under supervision of KARI. I would like to express my appreciation for Dr. William Warmbrodt, the chief of Aeromechanics branch who inspired the motivation for this research. I would like to thank Witold Koning leading the group with his unlimited support and kindness during my internship, as well as Esma Sahin for her active role as a senior member. My research was also possible because of Shirley Burek for the branch logistics, Eduardo Solis for 3D CAD model instructions, Robert Dueball and Natasha Barbely for theoretical background, and Suhyun Ock and Desireemoi Bridges for coordinating NASA I^2 program.

I also would like to thank my advisor, prof. Phillip J. Ansell, for his insights and advice throughout my research and demonstrating operations of critical equipment for both hardware and software during the experiment and simulations. I would like to thank prof. Ganesh Rajagopalan of Iowa State University and Luke Novak of Sukra Helitek for their support of the computational simulation program usage and license. I would like to thank my group members and fellow graduate program students, especially Rohit Gupta, Georgi Hristov and Aaron Perry for their help during my experiment, as well as James Favale and Branden Kirchner for their advice on particle image velocimetry.

Finally, I would like to thank my wife, and the best friend, Haedeun 'Haeley' Park for her endless support for both my professional career and life in general.

Table of Contents

List of Tables

List of Figures

Nomenclature

List of Symbols

$\mathbf{C_T}$	=	coefficient of thrust
V_∞	=	freestream velocity
$\mathbf{V_{tip}}$	=	rotor blade tip velocity
A	=	rotor disc area
R	=	rotor radius
T	=	thrust
Tu	=	turbulence ratio
Ω	=	rotor's rotational speed in rad/s
θ	=	rotor blade pitch angle
ρ	=	air density
β	=	crosswind angle

List of Abbreviations

CAD	=	computer aided design
CFD	=	computational fluid dynamics
DNS	=	direct numerical simulation
GUI	=	graphical user interface
JVX	=	Joint-service Vertical Take-off/Landing Experimental Aircraft Program
KARI	=	Korea Aerospace Research Institute
LES	=	large eddy simulation
PIV	=	particle image velocimetry
PTUAV	=	practical tiltrotor unmanned aerial vehicle
PWM	=	pulse width modulation
RC	=	radio control
RotCFD	=	rotorcraft computational fluid dynamics
RotUNS	=	rotorcraft unstructured grid simulation module
SIMPLER	=	semi-implicit method for pressure-linked equations revised
SLA	=	stereo lithography apparatus
TRAM	=	tiltrotor aeroacoustics model
UAV	=	unmanned aerial vehicle
UIUC	=	University of Illinois at Urbana-Champaign
URANS	=	unsteady Reynolds averaged Navier-Stokes equations
VTOL	=	vertical take-off/landing

Chapter 1

Introduction

1.1. Introduction of Tiltrotor Aircraft

Since the 1930s, aerospace and aviation industries have demonstrated great interest in the concept of tiltrotor aircraft, and recent technological improvements have allowed this concept to be realized. More recently, experimental tiltrotor aircrafts have been developed through flight-testing to full production and operation, including the Bell/Boeing V-22 Osprey. With improvements to technical readiness, in terms of stability, practicality and efficiency, tiltrotor aircrafts offer great potential for aviation purposes across military and civilian applications. This study investigates the complex flow interactions and the associated aerodynamic performance impacts of a tiltrotor aircraft's wing/rotor configuration. In particular, this chapter introduces background information of tiltrotor aircraft development history to provide context for understanding this study's objectives.

1.1.1. Historical Review of Tiltrotor Aircraft

Although it remains uncommon in modern aviation use, the tiltrotor system's roots began in the early stages of aviation history. In the 1920s, many flying vehicles offered the possibility of combining horizontal flying and vertical take-off capabilities in a single aircraft. For example, there was Henry Berliner's biplane with a fixed vertical rotor [1]. George Lehberger first introduced the tiltrotor aircraft concept with an actual conversion mechanism. He filed patent in

May 1929. It illustrated that a simple mechanical joint axle could rotate two different rotors and convert the direction of the rotor [2].

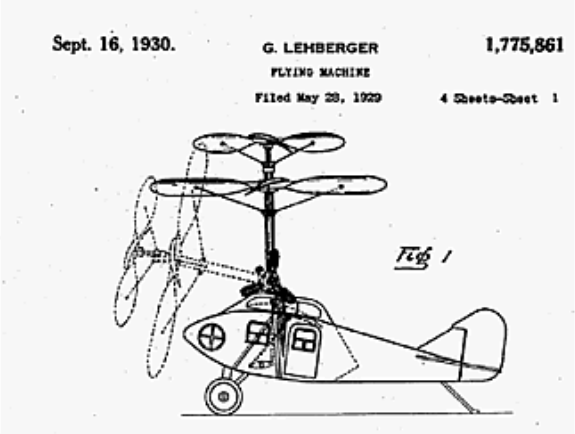

Fig. 1.1. George Lehberger's patent illustration of a tiltrotor flying machine [2]

It then took over 20 years after this conceptual development for an actual tiltrotor vehicle to be developed that would fly. Transcendental Aircraft Corporation of the U.S. built a Model 1-G and initiated its flight test in 1954. Although this aircraft program was short-lived—after only 3 years, the U.S. Air Force withdrew funding for further development of the project—the Transcendental Model 1-G and Model 2 served as the first successful model of a flight-mode conversion system in the tiltrotor aircraft [3].

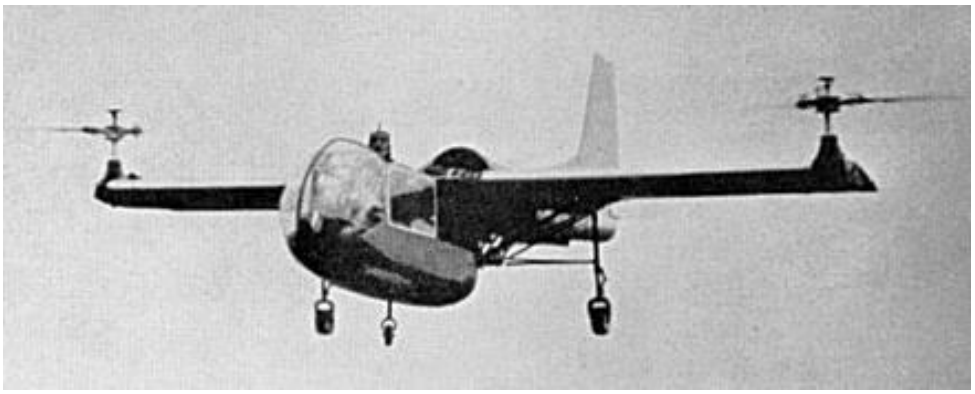

Fig. 1.2. Transcendental Model 1-G experimental tiltrotor aircraft in its hover flight during test phase [3]

In 1953, Bell Helicopter built the experimental XV-3 tiltrotor aircraft. It underwent regular flight-testing until 1966. During the flight-test phase, various technical improvements were made, such as: understanding the rotor dynamic instability problem in its early phase, analyzing the complex rotor/pylon/wing assembly system, and identifying the technical challenges of hover-to-cruise mode conversion. The significance of the XV-3 program served a crucial function for the next generation tiltrotor design. Although, the tiltrotor concept remains a difficult system to implement due to unresolved structural durability and inefficiency issues [1].

Fig. 1.3. XV-15 experimental tiltrotor concept aircraft in hover flight at NASA Dryden Research Center [4]

In 1971, Bell Helicopter, along with the U.S. Army (as a primary contractor), and NASA Ames Research Center (as a major test bed), began development of the XV-15 experimental aircraft. The building process was completed in 1977, and the aircraft performed its first flight. The XV-15 officially became the first tiltrotor aircraft to successfully operate in the world's first operational vertiport located at the Dallas Convention Center in Texas. The successful legacy of the XV-15 program initiated the JVX program, serving as the "brain child" of the Bell Boeing V-22 Osprey tiltrotor aircraft. Because of its VTOL capability, along with an efficient cruise flight mode, the V-22 Osprey proved its value for U.S. Marine and U.S. Air Force unit deployment in

combat zones. Indeed, this aircraft continues an active role in military operations since its delivery in December 2015 [5].

1.1.2. Advantages of Tiltrotor Concept over a Conventional Aircraft

Currently, conventional fixed-wing aircrafts and rotorcrafts, such as helicopters, are widely used in both military operations and civilian aviation. A conventional fixed-wing aircraft is popular in commercial flights because of its fuel efficiency and long-operation range. However, conventional aircrafts require an airport operating take-off and landing runways with sufficient length for the aircraft's operational requirements. The operational capabilities of these aircraft are limited to forward flight direction in order to generate sufficient lift in the air. Therefore, the fixed-wing aircraft in commercial flights is suitable for commercial transport airliners or regional jet operations.

The helicopter is widely used in military and civilian aviation for its flexible flight capability. Its VTOL, as well as its hovering characteristics, are suitable for rescue missions, medical transport, and combat force deployment in battle zones. However, due to the main rotor's aerodynamic inefficiency as a lift mechanism for cruising, the operational range of a helicopter is extremely limited. Moreover, its maximum cruise speed is nearly one third of conventional fixed-wing jet aircraft in general aviation.

The tiltrotor aircraft overcomes the range and speed limitations of the helicopter by directing its rotors toward the forward flight direction and operating in the form of a conventional fixed-wing aircraft. Meanwhile, it still possesses the VTOL, as well as the hovering characteristics, of the helicopter when directing its rotors vertically. Although the range and maximum speed of tiltrotors are not currently on par with fixed-wing aircrafts, tiltrotors'

versatility ranges between the fixed-wing aircraft and the helicopter. Table 1-1 compares the mission performance parameters of a V-22 Osprey tiltrotor aircraft model in comparison to a UH-60 Blackhawk helicopter to a Gulfstream G650. This offers a representative example of a modern fixed-wing jet aircraft and the U.S. Army's main carrier helicopter in use for cargo and force deployment missions. This comparison clearly indicates the tiltrotor aircraft's potential in the future, as it can fill in the gap between the fixed-wing aircraft and the helicopter for purposes of civilian aviation.

Table 1-1. Aircraft performance comparison for three different vehicle concepts

	Conventional Fixed-Wing	**Tiltrotor**	**Helicopter**
Aircraft Model	Gulfstream G650	V-22 Osprey	UH-60 Blackhawk
Range (nmi)	7,000	879	320
Maximum Speed (kn)	530	275	159
Cruise Speed (kn)	488	241	150
Service Ceiling (ft)	51,000	25,000	19,000
Passenger Capacity	11 - 18	24 - 32	11
Cargo Capacity (lbs)	6,500	20,000	2,640
VTOL/Hover	No	Yes	Yes

However, multiple obstacles remain for the industry to overcome in order to make a tiltrotor concept feasible at the civilian level. First, conversion from hover mode to cruise flight mode, or vice versa, is known for turbulent flow interactions between the rotor and an aircraft structure. These interactions make the vehicle difficult to control, producing a requirement of a highly complex control system. Tiltrotor aircrafts also require higher fuel consumption rates in comparison to the helicopter during its hover mode. The reason is due to larger vertical drag, as will be discussed in the Research Objectives section. Understanding the dominant aerodynamic characteristics, particularly the interactions between rotors and wing structure, is key to enabling more efficient tiltrotor configurations for civilian applications.

1.2. Research Objectives

1.2.1. Fountain Effect and Tiltrotor Performance

A typical tiltrotor aircraft has two rotors installed at the tip of each side of a main wing. Due to the main wing being directly located under two rotors, a vertical drag called download occurs, and previous studies on wing/rotor aerodynamic interactions indicate that this download contributes up to a 15% loss of the total rotor thrust [6] [7] [8]. This decrease is almost four times larger than the download from a typical helicopter's fuselage/rotor interactions, which is typically found to be 4% of the total rotor thrust [9]. The main cause for the much higher download of the tiltrotor wing/rotor configuration is the flow's momentum change on top of the wing structure and tip of two rotors, causing an air flow circulation, known as "the Fountain Effect" [10]. Fig. 1.4 visualizes the fountain effect on V-22 Osprey [7]. Komerath et al analyzes that the fountain effect accounts for 50% of the download during hover flight [10].

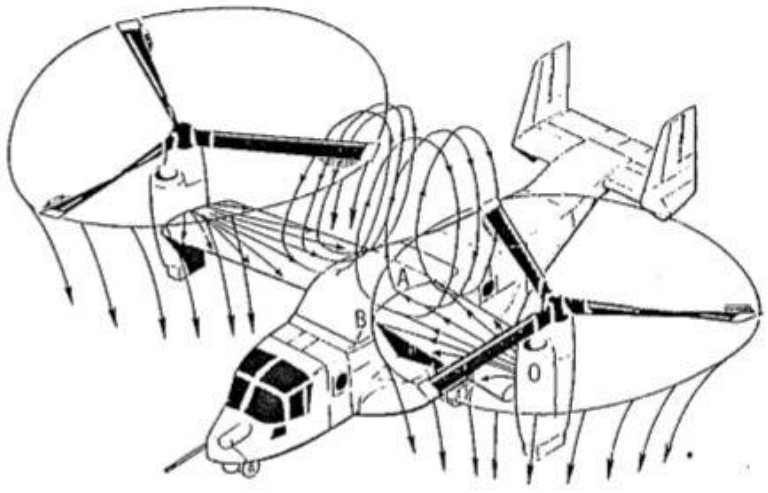

Fig. 1.4. Visualization of the fountain effect on V-22 Osprey tiltrotor aircraft [7]

1.2.2. Studying Aerodynamic Interactions of Wing/Rotor in Crosswind

A number of previous studies focused have on wing/rotor's aerodynamic interactions involving tiltrotor configurations in hover flight to determine download and flow control methods for mitigating download effects. Felker et al. conducted a flow circulation control method experiment to reduce the download caused by rotor and wing in hover [11]. Johnson et al. utilized a TRAM at NASA Ames Research Center to extensively study rotor and wing body interactions in addition to overall performance with downloads and structural loads [12]. McVeigh et al. successfully visualized the fountain effect on top of a full-scale V-22 aircraft experimentally, using colored smoke and tufts as visualization methods, which favorably compared to a VSAERO CFD simulation [7]. Potsdam et al. further investigated the various aeromechanics phenomena of a V-22 at low-speed flight with headwind, crosswind, and tailwind, during critical azimuth flight-testing, with a comparison to simulations from the OVERFLOW-D Navier-Stokes CFD code [13]. All previous experimental studies mentioned in this section require expensive large-scale wind tunnel facilities, custom-designed outdoor test stands, or actual vehicle's test flight for experiments. Similarly, simulations using high-fidelity CFD programs are computationally demanding, requiring a high computing budget. The primary objectives of this study, therefore, focus on a scaled wing/rotor model. It is tested in a sub-scale wind tunnel with a mid-fidelity CFD program, which demands a relatively lower computing power to run simulation cases. Simulated freestream velocity conditions and crosswind angles of the model are chosen to simulate moderate to extreme flight conditions in hover mode. Finally, results are compared to a series of wind tunnel tests to replicate those freestream conditions and crosswind angles used in CFD.

Chapter 2

Experimental Methods

The study involves a tiltrotor's wing/rotor configuration designed to properly test the model in both a hover flight condition and a crosswind condition replicated in the wind tunnel. The wing/rotor configuration has two rotors, and each individual rotor's thrust was measured using a load cell. Each rotor's rotational speed and blade pitch angle were designed to be controlled electronically, and the design's details are presented in Section 2.1. Replicating crosswind conditions using the wind tunnel is discussed in Section 2.2. To visualize the fountain effect's flow characteristics in a hover flight condition, a PIV experiment was designed using a high-power laser and optical components fixed on the optics table. Arrangement of an optical set-up is presented in Section 2.3. To validate experimental results acquired from both the hover flight test and the wind tunnel test, CFD simulations, using a rotorcraft-specific CFD program, were performed on desktop-level computers. Simulation conditions are discussed in Section Chapter 3.

2.1. Tiltrotor Wing/Rotor Configuration Model Construction

A tiltrotor wing/rotor configuration model was designed and constructed for both wind tunnel tests and PIV flow field measurements. Due to the size of the testing section of the sub-sonic wind tunnel at UIUC, the configuration was scaled down and prototyped to avoid wall effects and ground effects during the test. A virtual 3D model of the wing/rotor configuration for

CFD simulations was also designed as a simplified version of the experimental model to aid mesh grid generation with major components closely replicated.

2.1.1. References of Previous Studies in Tiltrotor Aircraft Models

Numerous studies on tiltrotor concepts investigated actual aircraft models with full-scale performance parameters provided. For instance, Felker and Light studied wing/rotor interactions, using 0.658 scale V-22 semi-span wing and rotor on a test rig with tufts and colored smoke as visualization tools [6]. Moreover, KARI developed a 60% scale model PTUAV for a full-scale Smart UAV project, as shown in Fig. 2.1 [14].

Fig. 2.1. Practical tiltrotor UAV under KARI Smart UAV

As with the XV-15 experimental tiltrotor aircraft discussed in Section 1.1.1, the performance parameters of three different tiltrotors were reviewed, as shown in Table 2-1. Specifically, rotor radius, wingspan, and rotor tip velocity are three major parameters reviewed closely to understand scaling effects on the full-scale model.

Table 2-1. Specifications of tiltrotor performance for three models used for parameter study

	Rotor Radius (m)	Wing Span (m)	Number of Blades	Rotor RPM in Hover	Rotor Tip Speed (m/s)	Disc Loading (kg/m^2)	MTOW (kg)
V-22	5.8	14	3	412	250.24	102.23	27,400
XV-15	3.81	9.8	3	589	235	73	6,000
PTUAV	0.93	3	3	1600	155.82	31.3	180

For the wind tunnel testing, only the main wing, two rotors and pods were scaled. The intention was to study the fountain effect and influence of the crosswind. The dimensions of the wind tunnel test section are 3x4 ft, and the model was configured to fit in the test section with clearance to avoid wall effects. It is well known in regards rotorcraft aerodynamics that ground effects can significantly change the efficiency and performance of rotors. To avoid the ground effect, previous studies have demonstrated that a clearance of, at minimum, twice the radius length of a rotor is required for the model out of ground effects [15]. All of these design parameters limited the size of the experimental model to a RC-scale helicopter, typically used for hobby purposes. Among the three tiltrotor aircrafts studied as references for scaling, the V-22 and XV-15 produce a rotor tip speed V_{tip} higher than 200 m/s. This rate is not feasible for the scaled experimental model, due to the extreme mechanical and electrical requirements of a high rotor RPM to match the tip speed on a sub-scale model. Therefore, KARI's PTUAV was chosen as the main reference model for this study. Notably, all three tiltrotor aircrafts studied for scale reference have triple-blade rotor systems.

2.1.2. Rotor Mechanical System Adaptation Using a RC-Scale Helicopter Model

A rotor configuration should be configured with control of both the rotational speed Ω and the blade pitch angle θ to vary the amount of thrust each rotor generates for different pitch angle conditions with a fixed V_{tip}. The coordinate system of the rotor in Fig. 2.2 shows the

reference axis of motion for Ω, and the cross-section of the blade shown in Fig. 2.3 shows the reference plane and axis of the blade that produces θ.

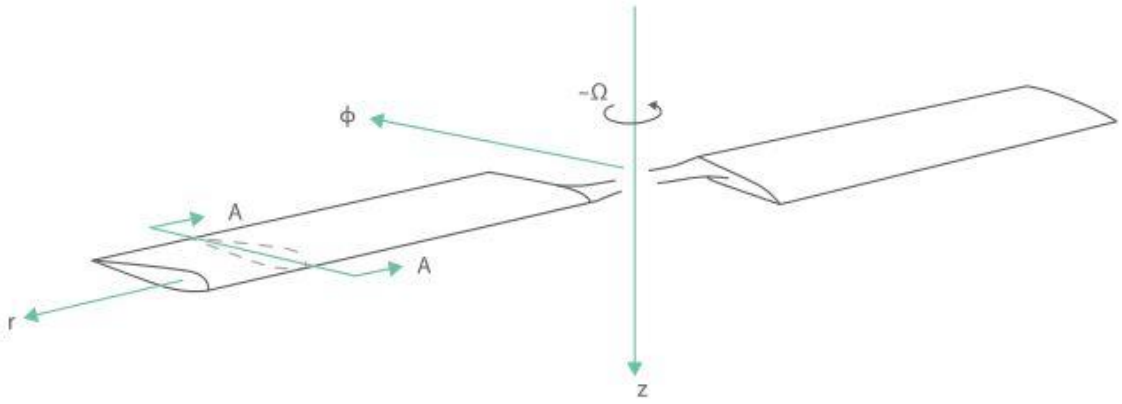

Fig. 2.2. Rotor and coordinate system [16]

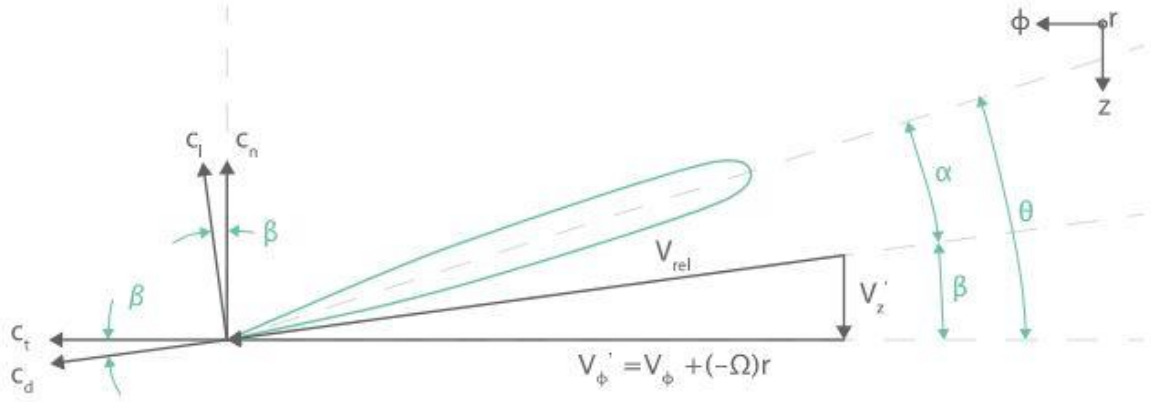

Fig. 2.3. Blade section nomenclature [1]

Considering the size of the wind tunnel test section, an RC-scale helicopter model with a rotor size radius of 200mm was deemed the most suitable system to be modified and fitted for the experimental configuration. To obtain control over the blade pitch angle and the rotor's rotational velocity, multiple electric helicopter models—with a swash-plate mechanism and an electronic speed controller—were studied. A Walkera 4F200LM model met all required conditions stated above, and two units were acquired for modification. A photograph of the Walkera 4F200LM model helicopter is shown in Fig. 2.4.

Fig. 2.4.Walkera 4F200LM radio control model helicopter [17]

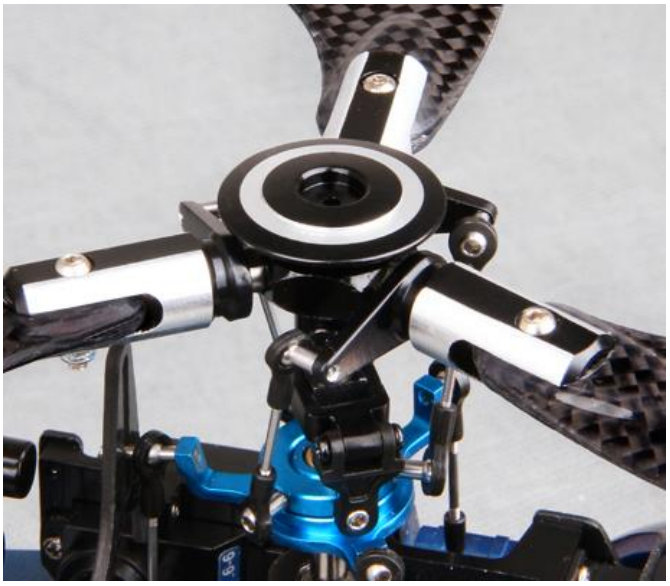

Fig. 2.5. 3-point swash-plate mechanism of the model helicopter rotor [18]

The Walkera 4F200LM model helicopter has a triple-blade rotor system. It is equipped with a 3-point swash-plate mechanism, as shown in Fig. 2.5. Each point of the swash-plate system is connected to a digital servo that may be controlled using PWM signals (through an RC specific receiver-transmitter device), or an Arduino circuit board with LabView software interface. The details of the control configuration will be discussed in Section 2.1.4.

The model blades and frame structure were modified in order to develop the sub-scale experimental model. Each blade was cut to a 5-in radius in order to fit within the wind tunnel test section, while still providing a 5-in wall clearance to avoid wall effects. The battery compartment of the main body panels was cut to leave only the mechanical compartment of the model, as shown in Fig. 2.6.

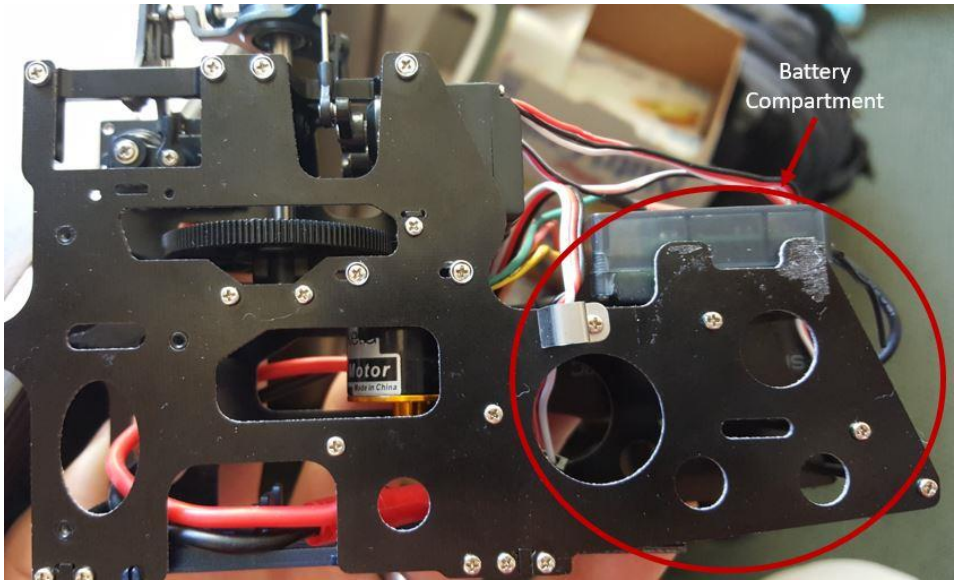

Fig. 2.6. Main body modification to reduce the mechanical gearbox size for pods

2.1.3. 3D CAD Process and Prototyping

A pair of pod fairings was designed to enclose the mechanical system of the modified Walkera 4F200LM model helicopter. The pod was configured to hold three digital servos, a motor, a rotor shaft (connected to a main spur gear), an electronic speed controller, and bearings. The pods were designed to be externally fixed onto a load cell for thrust measurement, as discussed in Section 2.1.4. One of the three servos, controlling a swash-plate, was exposed on the side of the main body panel. As a result, the pod design also has a rectangular hole that fits the servo body. A slot for the wing connector was also implemented to the pod design. The rectangular hole and the wing connector slot are shown in Fig. 2.7.

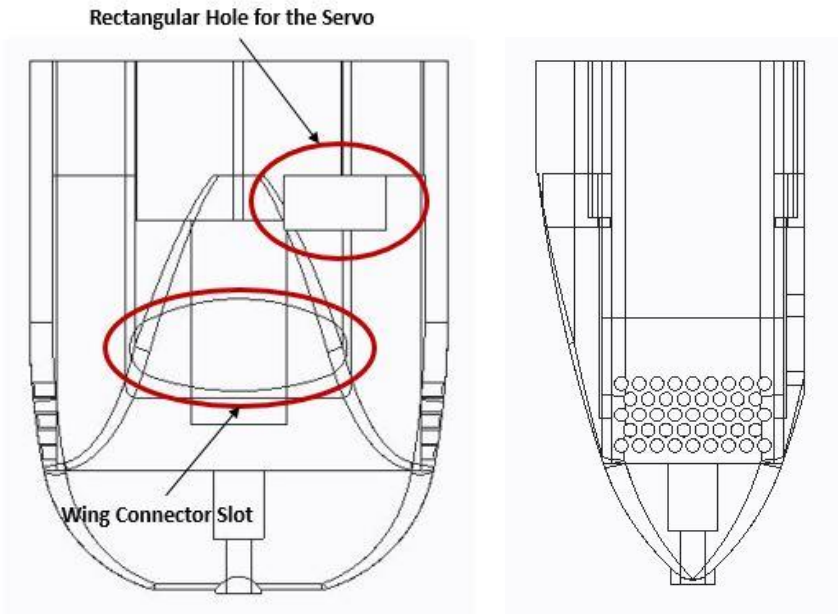

<Front View> **<Side View>**

<Bottom View> **<3D Rendered Image>**

Fig. 2.7. Pod design in 3D CAD program

A wing connector component was designed to serve as a connecting point between the pod and the wing plate. The wing was designed using a transparent Plexiglas plate to allow the laser sheet to pass through during PIV experiments, as discussed in Section 2.3. The wing connector was designed to attach to a pod on the outboard side, while also holding the Plexiglas wing plate with a bolt and nut through a set of holes on the connector and the wing plate. The wing connector design in the 3D CAD program is shown in Fig. 2.8.

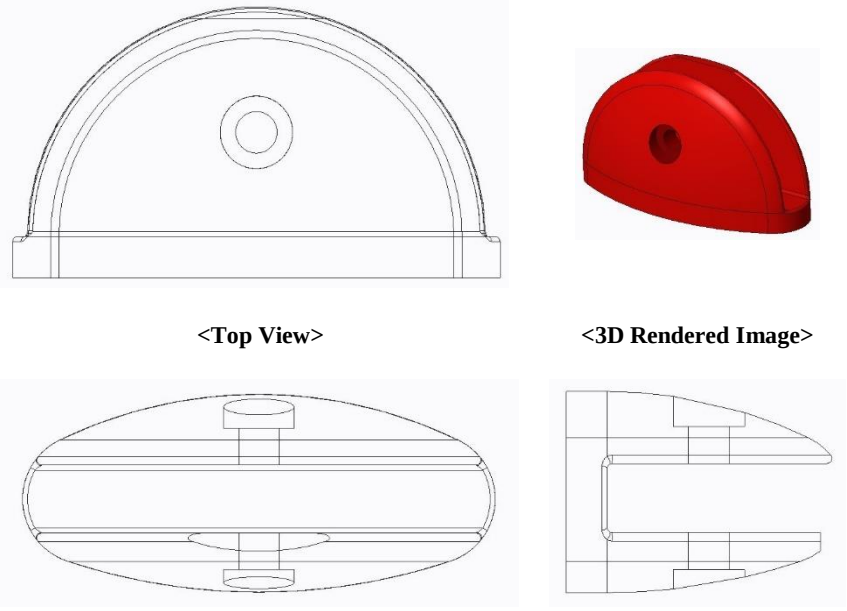

Fig. 2.8. Wing-to-pod connector in 3D CAD program

A rotor cone was designed to replicate the propeller spinner of a typical tiltrotor aircraft's rotor system. The Walkera 4F200LM model helicopter rotor has a hub plate with a 1.5mm size threaded hole. Thus, the rotor cone was configured with a hole along its rotational axis, which was held by the 1.5mm bolt on top of the rotor head. The rotor cone design in the 3D CAD program is shown in Fig. 2.9.

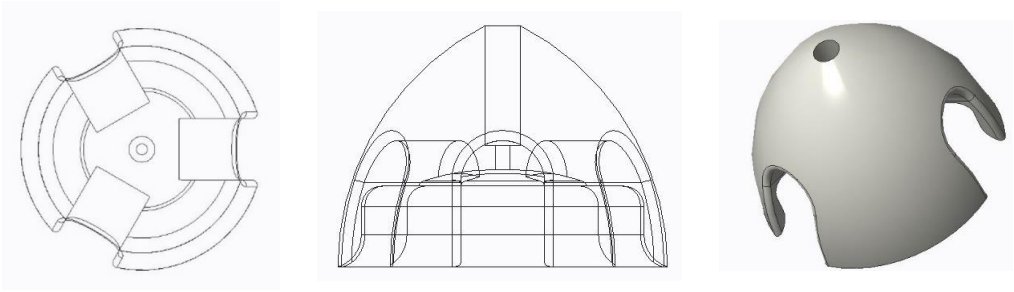

Fig. 2.9. A rotor cone replicating the propeller spinner of a tiltrotor aircraft in 3D CAD program

Prototyping each component was completed using an Ultimaker 3D printer. Based on the initial prototypes, modifications were developed to produce the final design. Then, the final components were printed, using a Viper SI SLA 3D printer, in the Ford Rapid Prototyping Lab at UIUC Mechanical Engineering Department. The assembled wing/rotor system was mounted to two 0.5×12-in aluminum cylindrical posts. A base plate was fabricated to interface with the wind tunnel test section rotational balance. Then, the aluminum cylindrical posts were attached to the base plate to hold the pods and rotors in place. The Plexiglas wing plate and the base plate were cut using a laser cutter. The thickness of the Plexiglas was 0.25 in. The Plexiglas wing plate and the base plate are shown in Fig. 2.10.

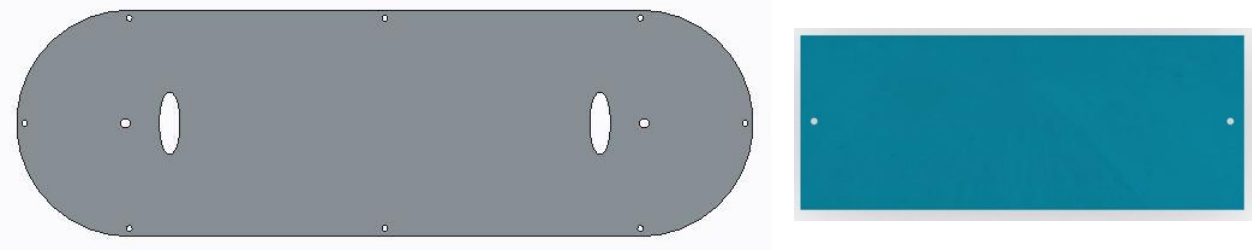

<Base Plate> **<Wing Plate>**

Fig. 2.10. Plexiglass wing plate and a base plate that fits in the wind tunnel test section's rotational balance

The final assembly of the wing/rotor configuration for the wind tunnel tests is shown in Fig. 2.11 and Fig. 2.12. The wing/rotor configuration was mounted 18in above the base plate, placing the rotor location well above the 2-radius minimum height from the ground to avoid ground effect. The distance between the centers of the two rotors measured 15in, which corresponds to a 3-radius distance between the rotors. The full horizontal dimension of the wing/rotor configuration from right end to left end is 25in, which leaves 6.5in clearance each on the right and left sides of the wind tunnel test section. This wall clearance is greater than a 1

radius length of the rotor. It aimed to alleviate expected wall effects during the testing. An overview of the rotor/wing configuration is shown in Fig. 2.14.

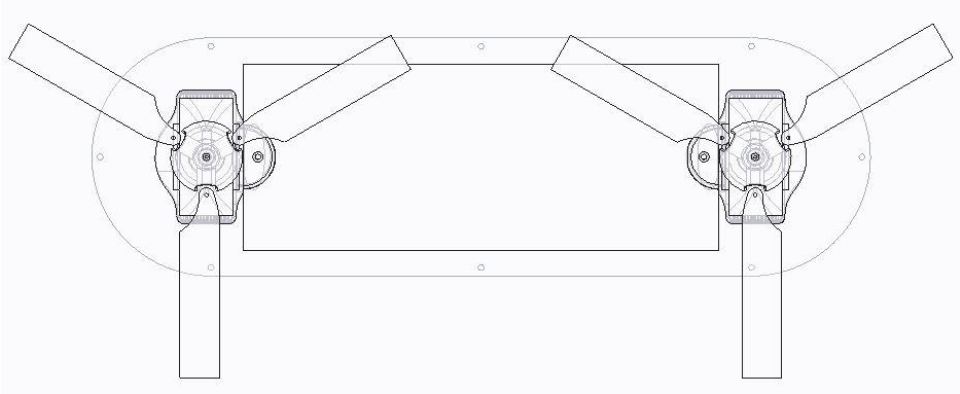

Fig. 2.11. Top view of the wing/rotor configuration in 3D CAD

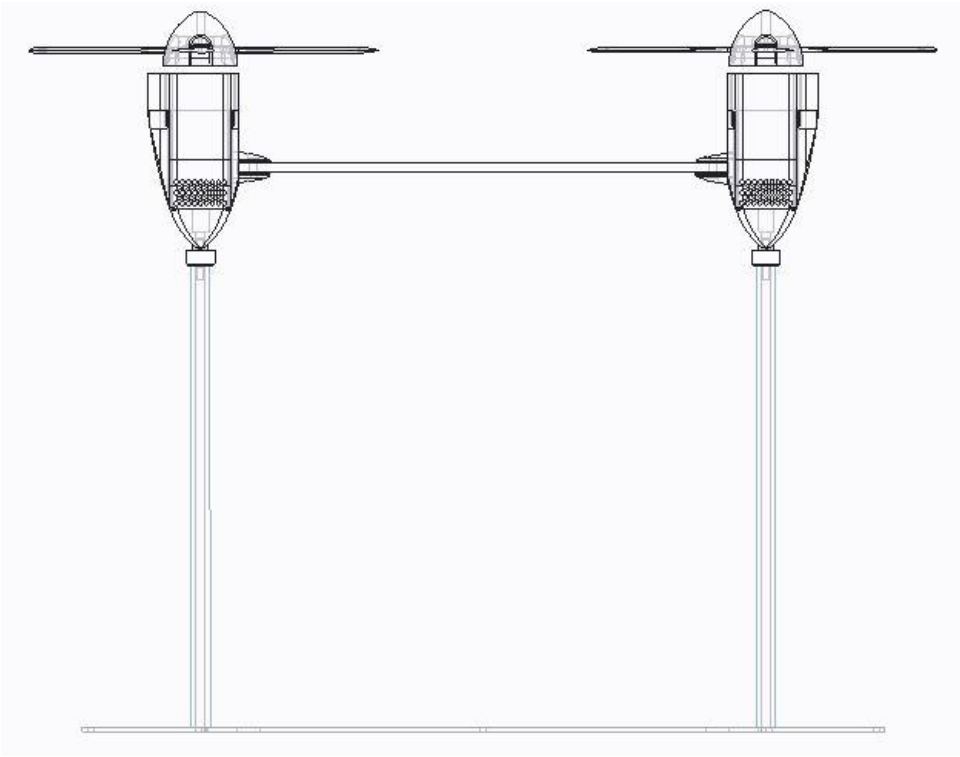

Fig. 2.12. Front view of the wing/rotor configuration in 3D CAD

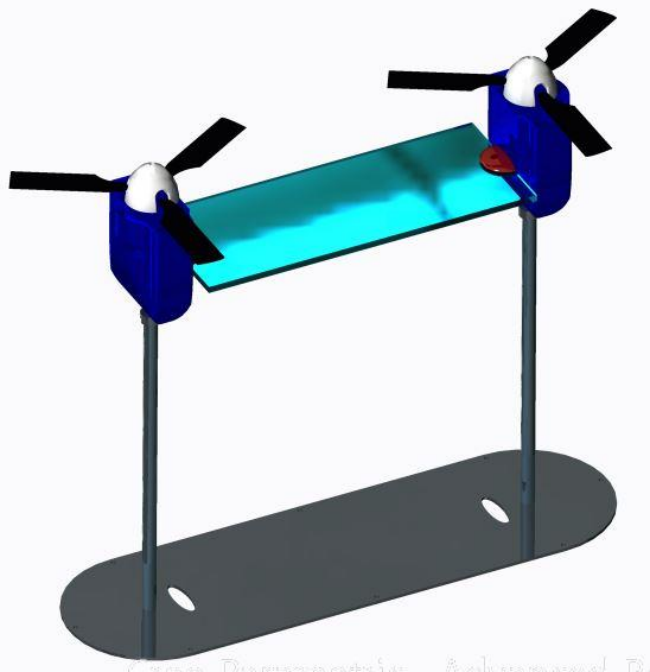

Fig. 2.13. Rendered view of the rotor/wing configuration for a wind tunnel test

2.1.4. Thrust Measurement and Control System

To compare the performance of the rotor assembly between the simulations and experiment, the thrust coefficient was used. To calculate the thrust coefficient from the rotor in different testing conditions, the thrust from the two rotors should be measured from the test rig. A thrust coefficient C_T equation of the rotor is shown in Equation (2.1) [15],

$$C_T = \frac{T}{\rho A(\Omega R)^2} \tag{2.1}$$

where T is a thrust measured from the two rotors, ρ is an air density, and Ω is a rotor's rotational velocity in rad/sec. To measure the thrust from two rotors directly, load cells were installed underneath the pods. The load cells are capable of comparing tension/compression measurements with a capacity up to 5 lbs. The load cells have threaded connectors on both sides of the unit as shown in Fig. 2.14. Moreover, one end of the load cell was attached to a heat insert,

which was installed directly on the mounting holes of the pods. The other end was locked on the aluminum cylindrical post, thus supporting the overall configuration.

Fig. 2.14. Cooper Instruments LPM-514 load cell

Some of the stock electronic components from the Walkera 4F200LM helicopter bundle package were replaced in order to maintain stable performance from the rotor's mechanical system. Servos were replaced with high-torque micro-servos, with a toque rate of 1.7 kg-cm. Motors were replaced with high performance brushless motors with a 5,400-kV rating, which produces 5,400 RPM/V of electrical supply voltage. The electronic speed controllers of the brushless motors were replaced with new units, having higher-maximum amperage rating of 60A. Specifications of these replaced components are stated in Table 2-2.

Table 2-2. Components for thrust measurement and rotor control system

Component	Specification	Product Information
Load Cell	Range: 0-5 lbs	Cooper Instruments LPM512-5
Servos	Torque: 1.7 kg-cm (6V)	Futaba S3114 Micro High-Torque Servo
Motors	Rotation: 5,400kv	Turbo Ace 354 Outrunner Motor
Electronic Speed Controller	Max Amp: 60A	Hobby King 60A Speed Controller

These electronic components were connected using wires and breadboards to an Arduino Uno micro controller, which was coupled to a LabView interface in order to control their functions during thrust data acquisition. A diagram of the wired components is shown in Fig.

2.15. Further, a programmed LabView VI interface is shown in Fig. 2.16. The VI interface uses a servo-control function to change the blade pitch angle. Another VI program controls the motor's rotational speed through a variation in the Arduino output signal to the speed controller. Servo calibrations were performed through a separate VI program along with a rotor blade angle gauge. The calibration VI interface is shown in Fig. 2.17.

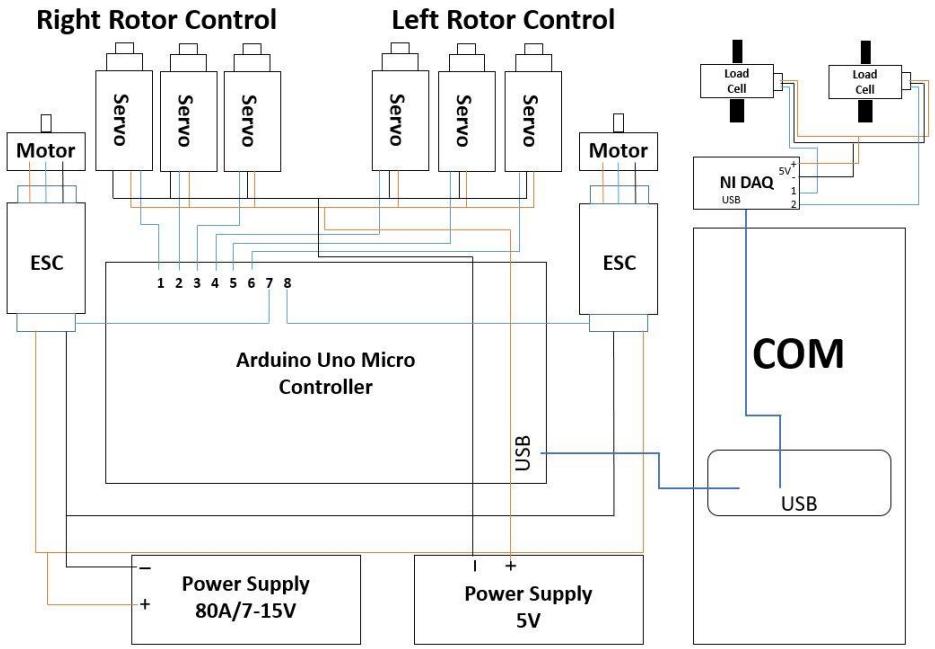

Fig. 2.15. Diagram of components wired to Arduino Uno micro controller and NI USB data acquisition board

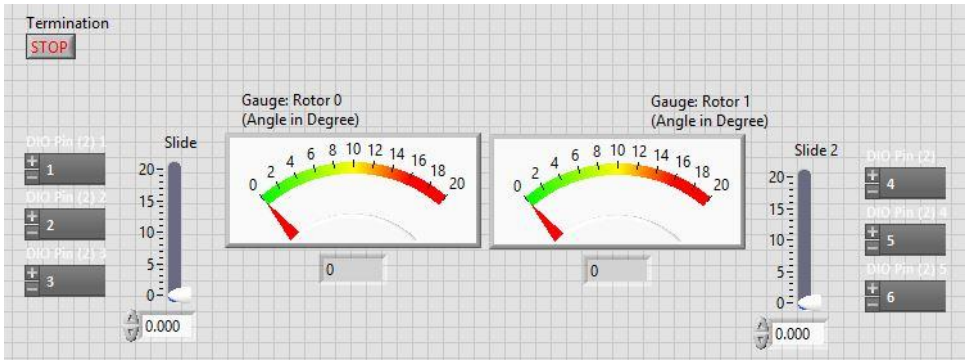

Fig. 2.16. LabView VI interface to control servos and motors of the wing/rotor configuration

Fig. 2.17. LabView VI interface for a servo calibration process

2.2. Experimental Set Up in Subsonic Wind Tunnel

A series of experiments were conducted on the tiltrotor wing/rotor model, as discussed in this section. To record data, a subsonic wind tunnel was utilized to test the wing/rotor configuration in different conditions of freestream velocity and across a range of crosswind angles. Post-processing of the obtained data was performed to interpret flow interactions between the rotor and wing in crosswind flight conditions and influences on the fountain effect.

2.2.1. Wind Tunnel Set-Up

The sub-sonic wind tunnel at UIUC Aerodynamics Research Laboratory is an open-circuit wind tunnel with a test section size of 3x4 ft with a low turbulence level ($Tu < 0.1\%$) [19]. The wind tunnel's internal control program allows flow velocity, or Re number, to be set within $\pm 1\%$. The test section is equipped with a rotating turntable that changes the angle between a test article and the direction of freestream velocity. This may be interpreted as a

crosswind angle for the purposes of this study. The rotating plate is also internally controlled with a feedback system that allows for precise angle control. A schematic illustration of the wind tunnel is shown in Fig. 2.18.

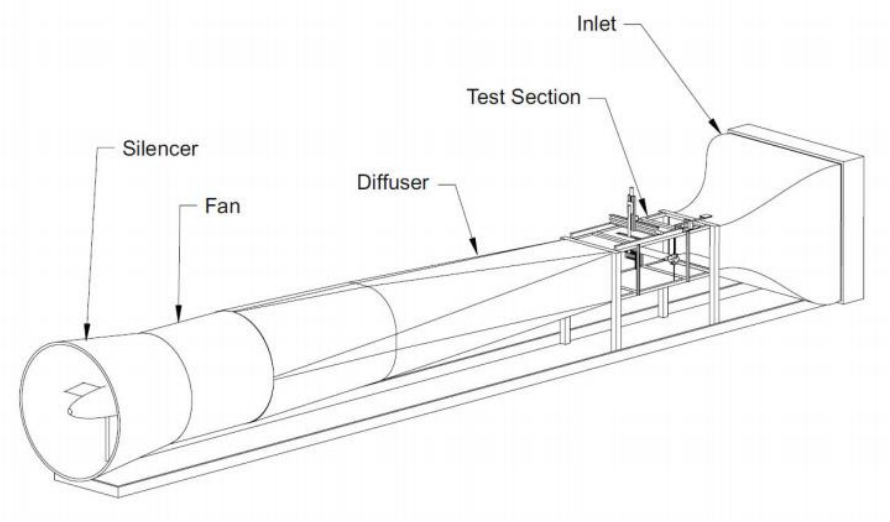

Fig. 2.18. Schematic of UIUC 3x4 ft sub-sonic wind tunnel in Aerodynamics Research Laboratory [19]

A crosswind angle of $\beta = 0°$ was defined with the wing/rotor configuration, facing directly toward the freestream, and generated within the wind tunnel test section. An angle of $\beta = 90°$ is produced when one of the rotors faces toward the freestream direction. Fig. 2.19 shows the reference of a freestream direction and a rotational axis of the wing/rotor configuration within the wind tunnel test section.

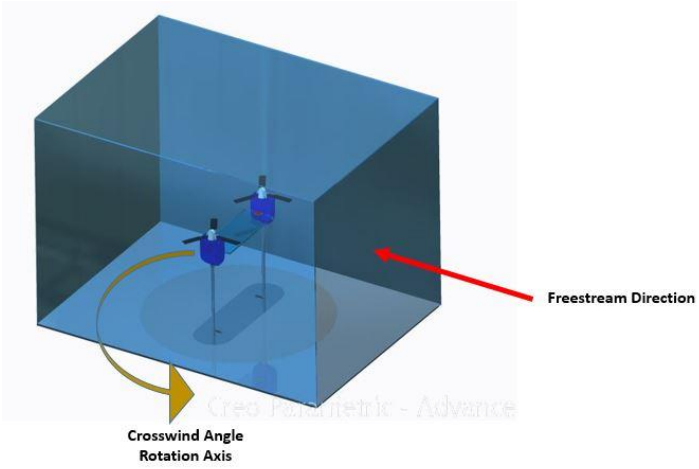

Fig. 2.19. Orientation of the wind tunnel freestream and crosswind angle rotation axis

To avoid wall effect and ground effect, the wing/rotor configuration is designed to maintain at a distance greater than a rotor diameter between the rotor tip and the sidewall of the wind tunnel. Further, a 1-foot gap from the wind tunnel floor to the load cells was installed underneath two pods as discussed in Section 2.1. The installed wing/rotor configuration for a wind tunnel test is shown in Fig. 2.20. Wires connecting servos, motors, and load cells were wrapped with electrical adhesive tape and given sufficient clearance to avoid load cell hindrance and to ensure accurate thrust measurements.

Fig. 2.20. Wing/rotor configuration model installed in the wind tunnel test section

2.2.2. Flow conditions and Experiment Condition Parameters

Three different flow speeds and three different blade pitch angles were defined for the wind tunnel tests. To consider the capacity of the motors driving two rotors, and to find an optimal value providing a sufficient V_{tip} to V_∞ in ratio, the V_{tip} of the two rotors were fixed at 60 m/s. Freestream velocities were defined to be $\frac{V_{tip}}{3}$, $\frac{V_{tip}}{4}$, and $\frac{V_{tip}}{6}$. Blade pitch angles θ were defined after conducting several preliminary tests. Crosswind angles ranged from 0°-90° with a 15° increment. These testing parameters are stated in Table 2-3.

Table 2-3. Experiment condition parameters for wind tunnel test sequence

Experiment Parameters	Values
Freestream Flow Speed (m/s)	10, 15, 20
Blade Pitch Angle(°)	5, 10, 15
Crosswind Angle(°)	0,15,30,45,60,75,90
Rotor Tip Velocity (m/s)	60

For each test sequence, one freestream velocity condition and one blade pitch angle were fixed. The crosswind angle of the test configuration was changed to record the thrust data, which was measured from the load cell. For one set of data, V_∞=15m/s was fixed and the blade pitch angles were varied to study thrust variations. For another set of data, θ =15°was fixed. Further, three different V_∞ conditions were varied in order to study the effect of a freestream flow for the tiltrotor configuration during a hover flight and in crosswind.

2.3. Flow Visualization Using PIV

A PIV experimental design was used to acquire the flow field data for the fountain effect of the tiltrotor's wing/rotor configuration. The same wing/rotor test configuration was assembled and installed on an optic table along with optical components. Seed particles for PIV were

introduced to the region of the wing surface where the fountain effect was anticipated to be evident. Further, a CCD camera was set to capture the motion of the seed particles, to study flow interaction between the rotor and the wing structure.

2.3.1. Hover Flight Test Rig

Before the PIV experiment was conducted, the wing/rotor configuration from the wind tunnel was tested. This test aimed to investigate the expected thrust value for a hover flight condition without freestream flow. A test rig was designed to enclose the wing/rotor configuration without interfering the flow induced from the two rotors. The base plate has multiple holes with a 1-in space among them. It was designed to match the hole-pattern of an optical table. An overview of the test rig is shown in Fig. 2.21.

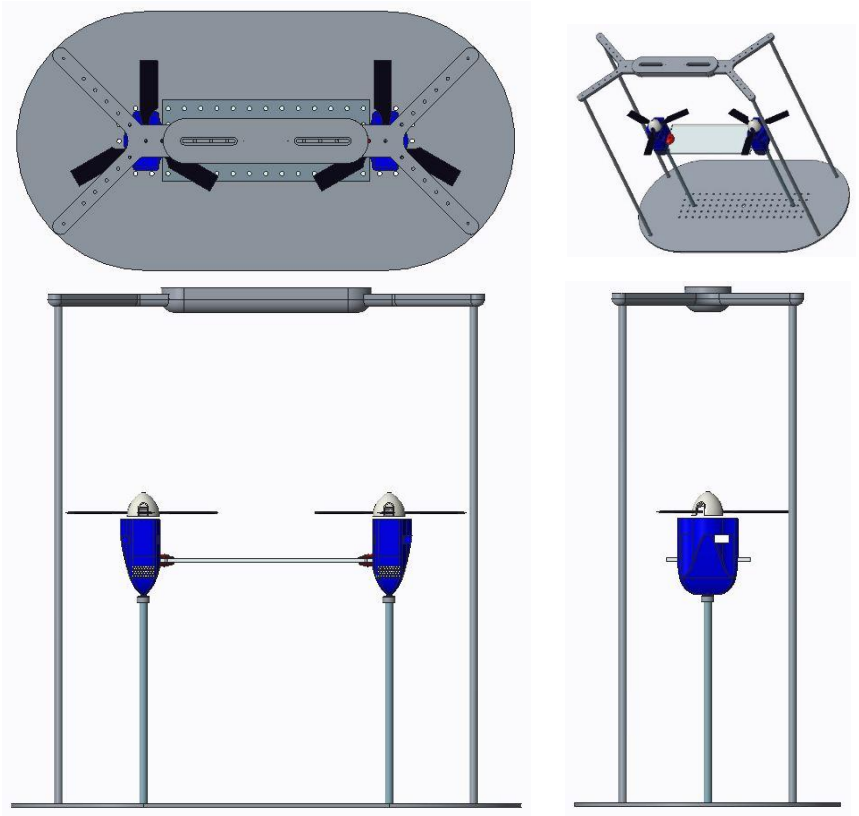

Fig. 2.21. Wing/rotor test rig for hover flight condition test and PIV experiment

A photograph of the experiment is shown in Fig. 2.22. It features two rotors, two load cells, an Arduino Uno (connected to electronic components for controlling the rotor speed and blade pitch angle), and the base plate (fixed to an optical table). $\theta = 5°$, 10°, and 15° were tested to measure the level of thrust from two rotors.

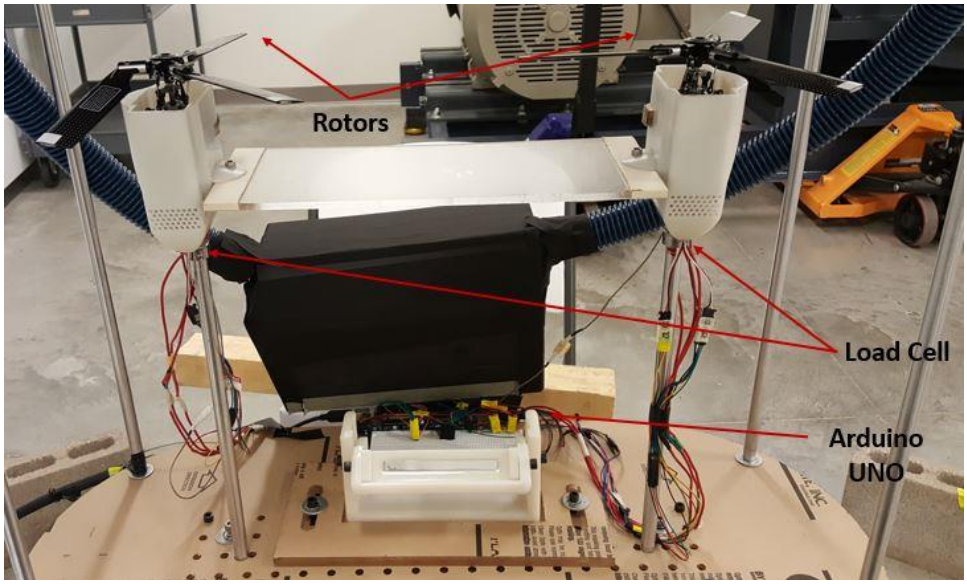

Fig. 2.22. Hover flight test rig fixed on an optics table

2.3.2. Optical Components Set-Up

To produce a laser sheet for the PIV experiment, a New Wave Research Solo 200XT high power laser was used for this study. The Solo 200XT laser generates a 200mJ laser beam at 532nm wavelength. To direct the laser beam, four different 532nm dichroic mirrors with a 100% reflection rating were fixed on an optic table. Then, the laser beam was passed through a cylindrical lens of $f = $-30mm, and two spherical lenses of $f = 20$mm and $f = 50$mm, were arranged to create a laser sheet. A rectangular mirror was installed directly underneath the Plexiglas wing plate to reflect the sheet up into the region between the rotors. The CCD camera was installed to capture the field of view across the mid plane of the wing and also to capture the

fountain effect. A diagram of the optical components design is shown in Fig. 2.23. PIV data were processed using LaVision Davis. The final component arrangement is shown in .

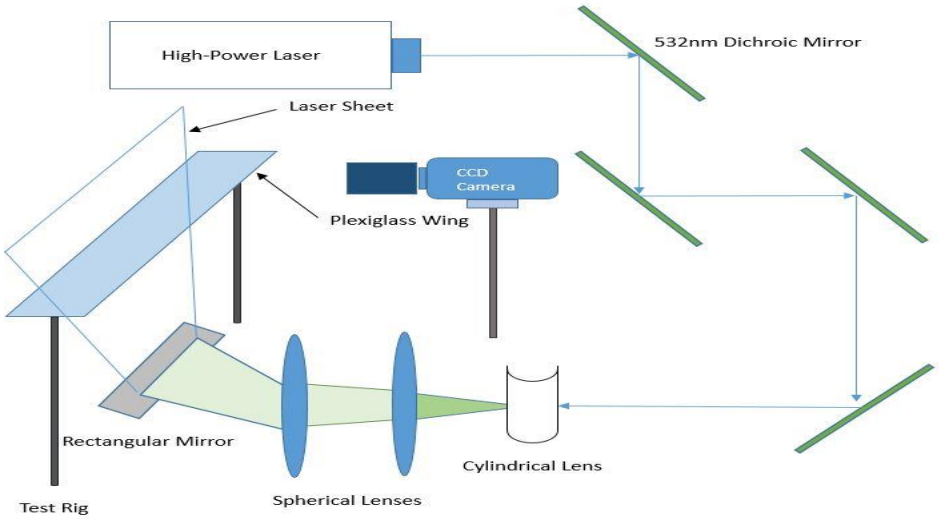

Fig. 2.23. PIV components set-up diagram

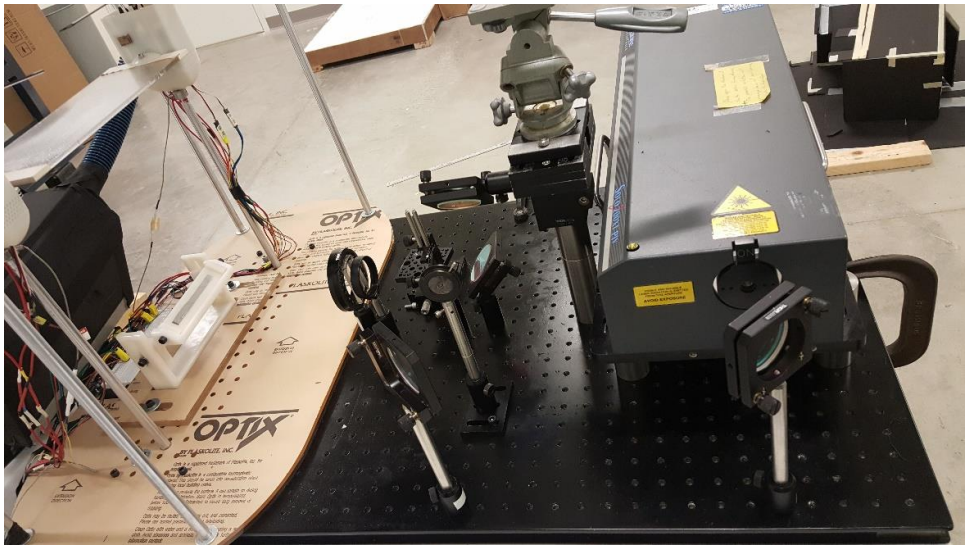

Fig. 2.24. Optical components ranged and fixed on an optics table for PIV

During PIV experiments, an oversaturation of the seeding particles from the smoke generator within the testing space became a major issue. To avoid oversaturation of the seeding particles, a confinement and mechanism to feed seeding particles locally to the area of interest was developed. The confinement was improvised with three black screens, which were made

from plastic panels. These panels were measured and cut to block the upper part of the testing region and to avoid flow interference. Then, holes were cut from the right and left sides of the confinement, and two flexible vacuum tubes were connected to each side. The vacuum tubes were connected at the other ends to combine the feeding system with a smoke generator. The 3D rendered image of this improvised system is shown in Fig. 2.25.

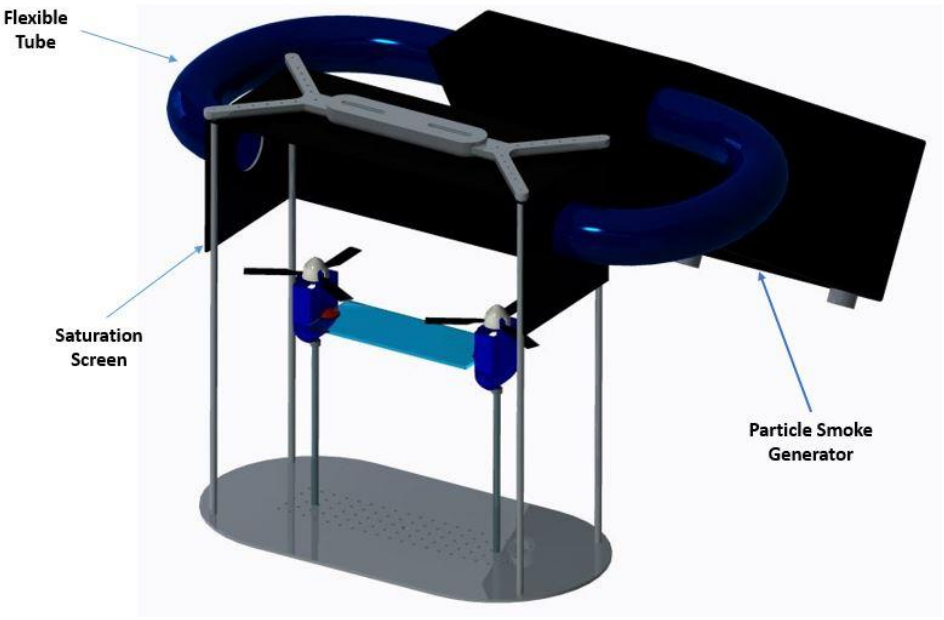

Fig. 2.25. Localized particle seed feeding system with confinement screens

The system was tested, and the oversaturation problem was solved. The new particle feeding system proved effective for providing better particle density and laser scattering to the CCD camera, capturing flow interaction with rotors and wing plate. An actual system installed onto the test configuration with a smoke generator is shown in Fig. 2.26 and Fig. 2.27. A background screen was installed to reduce reflections of the laser sheet across the testing room.

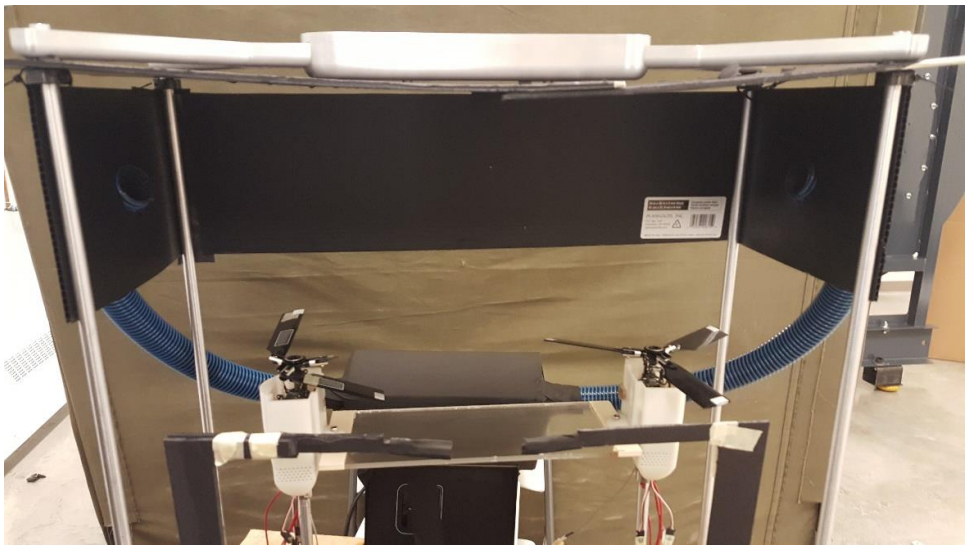

Fig. 2.26. Particle feeding system improvised to aid local saturation for visualization with a back screen

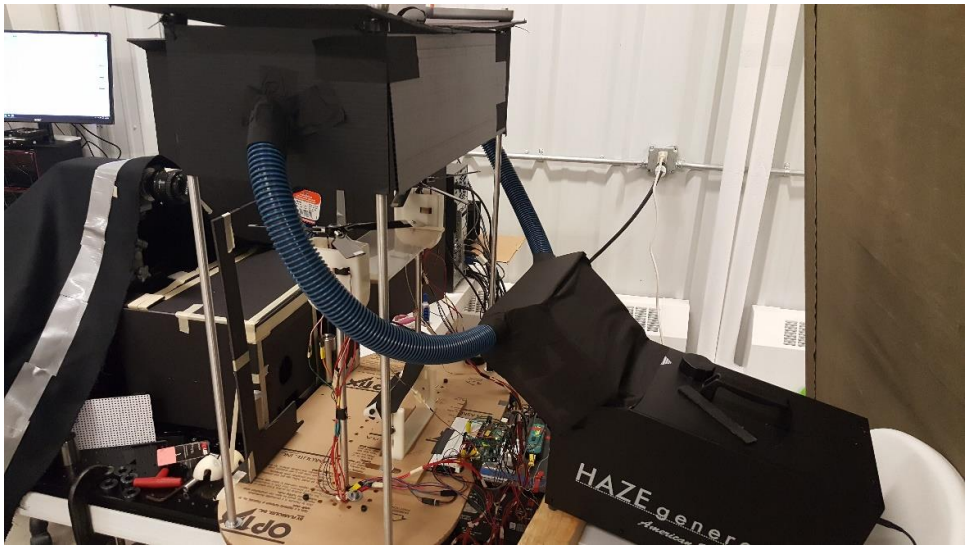

Fig. 2.27. Particle feeding system and smoke generator assembly

Chapter 3

CFD Simulation

In this study, a computational simulation of the unsteady flow interaction for a rotor in rotation was performed using a mid-fidelity computational fluid dynamics tool. RotCFD is the computational tool used to provide a representation of the flow interactions. The simulated tiltrotor configuration has two rotors, two pods, and a main wing assembly in hover mode. Simulations were conducted with parametric changes in freestream velocity, crosswind angle, and blade pitch angle to provide numerous variations in the hover flight conditions. The rotor's tip speed was kept fixed across all simulations.

3.1. Comparison of Different CFD Approaches

DNS, LES, RANS, and URANS are common approaches for viscous CFD simulation. These CFD approaches solve the Navier-Stokes equations numerically, where continuity and conservation of momentum are stated as:

$$\frac{\partial \rho}{\partial t} + \nabla \cdot \left(\rho \vec{V}\right) = 0 \tag{3.1}$$

$$\frac{\partial}{\partial t}\left(\rho \vec{V}\right) + \nabla \cdot \rho \vec{V}\vec{V} = \rho \vec{f} + \nabla \cdot \widetilde{\Pi}_{ij} + \vec{S} \tag{3.2}$$

where, ρ is the density of fluid, $\vec{V}$ is the velocity vector, $\vec{f}$ is the body force, $\tilde{\Pi}_{ij}$ is the stress tensor and $\vec{S}$ represents all external source terms [20]. The above equations may be expressed in incompressible, three-dimensional Cartesian system forms as follows:

$$\frac{\partial u}{\partial x}+\frac{\partial v}{\partial y}+\frac{\partial w}{\partial z}=0 \tag{3.3}$$

$$\frac{\partial(\rho u)}{\partial t}+\frac{\partial}{\partial x}\left(\rho u^2-\mu\frac{\partial u}{\partial x}\right)+\frac{\partial}{\partial y}\left(\rho uv-\mu\frac{\partial u}{\partial y}\right)+\frac{\partial}{\partial z}\left(\rho uw-\mu\frac{\partial u}{\partial z}\right)=-\frac{\partial p}{\partial x}+S_x \tag{3.4}$$

$$\frac{\partial(\rho v)}{\partial t}+\frac{\partial}{\partial x}\left(\rho uv-\mu\frac{\partial v}{\partial x}\right)+\frac{\partial}{\partial y}\left(\rho v^2-\mu\frac{\partial v}{\partial y}\right)+\frac{\partial}{\partial z}\left(\rho vw-\mu\frac{\partial v}{\partial z}\right)=-\frac{\partial p}{\partial y}+S_y \tag{3.5}$$

$$\frac{\partial(\rho w)}{\partial t}+\frac{\partial}{\partial x}\left(\rho uw-\mu\frac{\partial w}{\partial x}\right)+\frac{\partial}{\partial y}\left(\rho vw-\mu\frac{\partial w}{\partial y}\right)+\frac{\partial}{\partial z}\left(\rho w^2-\mu\frac{\partial w}{\partial z}\right)=-\frac{\partial p}{\partial z}+S_z \tag{3.6}$$

where, μ is the diffusion coefficient, and u, v, and w are the velocity components in three-dimensional Cartesian system in x, y, and z directions respectively,. S_x, S_y, and S_z are the external source terms in x, y, and z directions respectively.

DNS solves the Navier-Stokes equations directly to determine the velocity field $U(x,t)$ for one realization of the flow, including all turbulent length scales and time scales in the flow. Thus, DNS requires a large computational budget, reaching a level that is typically only accessible by modern supercomputers. This computational budget increases for higher turbulence Reynolds number Re_L and Taylor-scale Reynolds number R_λ. Pope expressed these two variables in terms of the number of modes at three directions N^3 and the number of time steps M as the following equation [21].

$$N^3M \sim 160Re_L^3 \approx 0.55R_\lambda^6 \tag{3.7}$$

Therefore, the magnitude of the computing budget demand is proportional to Re_L^3. The computing time can be calculated, assuming 1,000 floating-point operations per N^3M are required, and CPU calculation speed is 1 teraflop (10^{12} floating point operations/second) [21].

$$T_t = \frac{10^3 N^3 M}{10^{12} \times 60 \times 60 \times 24} \sim \left(\frac{Re_L}{8000}\right)^3 \tag{3.8}$$

where, T_t is the time in days for a 1 teraflops CPU to complete one simulation case. Using the equation above, Table 3-1 shows the computing time lengths required for different Reynolds number scales. The result indicates that DNS requires extremely high computing power and time for a relatively low Reynolds number. This is impractical for a rotorcraft aerodynamics simulation with high rotor tip speed.

Table 3-1. Required computing time for DNS approach in CFD simulation

R_λ	Re_L	N^3M	CPU	Time
100	1,500	1.1×10^{12}	20	min
200	6,000	5.2×10^{13}	14	hours
400	24,000	2.8×10^{15}	32	days
800	96,000	1.6×10^{17}	1,851	days

LES alleviates this high computational demand with a filtered velocity field $\bar{U}(x,t)$, representing the larger scale turbulent motion. The velocity field is resolved in space, calculating the large-scale turbulent flow structures and modelling only the smallest scales. LES reduces the amount of computing power required for simulation in comparison to the amount that DNS demands. However, LES requires proper filtering and grid application to guarantee its accuracy, which demands significant effort [22].

One major difference between RANS or URANS and LES is that RANS or URANS is a time-averaging approach instead of a space-averaging approach. For multiple time scales, RANS

and URANS consider the average of the velocity components of fluid in motion along with fluctuation, as shown in the following equations.

$$u = \bar{u} + u' \tag{3.9}$$

$$\bar{u} = \frac{1}{T_1}\int_{T}^{T+T_1} u\,dt \tag{3.10}$$

where, u is the velocity component, ū is the average value of the velocity component over a specific time span, and u′ is the fluctuation term of the velocity component. The averaged velocity component over multiple time scales, as expressed in the above equations, can be visualized with averaged velocity over time with a low-pass filter as shown in Fig. 3.1. Multiple time scales for construction of the velocity component in RANS/URANS equation Fig. 3.1, where $T_1 \ll T \ll T_2$ [23].

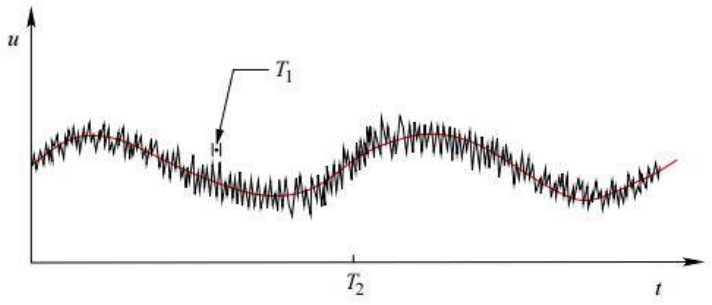

Fig. 3.1. Multiple time scales for construction of the velocity component in RANS/URANS equation [23]

Because of its time-averaging characteristics, RANS and URANS do not require as much computing budget as LES. N. Gourdain's study indicates that the computing-cost ratio from RANS equations to wall-resolved LES for an isolated compressor blade is about 10,000 at Re ≈ 10^6 [24]. However, this relatively low computing budget requirement compromises fidelity, especially in turbulence modeling. Therefore, RANS and URANS must be used carefully with a

proper time scale for averaging that is defined to prevent disagreement with experimental data within a reasonable range [23].

3.2. Theoretical Background of RotCFD

RotCFD was developed to specifically solve flow interaction for rotorcrafts using a relatively low computing budget, such as the processing power offered by desktop computers. RotCFD utilizes URANS as governing equations [20]. RotUNS is one of various modules within RotCFD that implements the URANS solver on a Cartesian unstructured grid with an Octree grid generation feature, to be discussed in Sec. 3.4 [25].

Also, RotUNS features the SIMPLER algorithm developed by Brian Spalding and Suhas Patankar. The advantage of SIMPLER is that it introduces an under-relaxation factor into the solver to iteratively obtain the correct flow field in agreement with both the continuity and momentum equations. This feature potentially lowers the computing budget for a simulation while maintaining a reasonable fidelity of the simulation data [26]. These reasons make RotCFD suitable as a CFD tool for this tiltrotor wing/rotor aerodynamic characteristics study. Turbulence modeling is performed using the κ- ε turbulence model, where κ is the kinetic energy, and ε is the turbulent dissipation [27].

RotCFD has a GUI that simplifies the process of simulation configuration and design, especially for the purpose of modeling a rotor in motion. It is user-friendly and appropriate for the current study because it narrows the simulation scope specifically to rotorcraft aerodynamics. GUI features include mesh control, rotor dimensions and specifications, body geometry implementation and adjustment, flow characteristics, and boundary conditions control, as shown in Fig. 3.2.

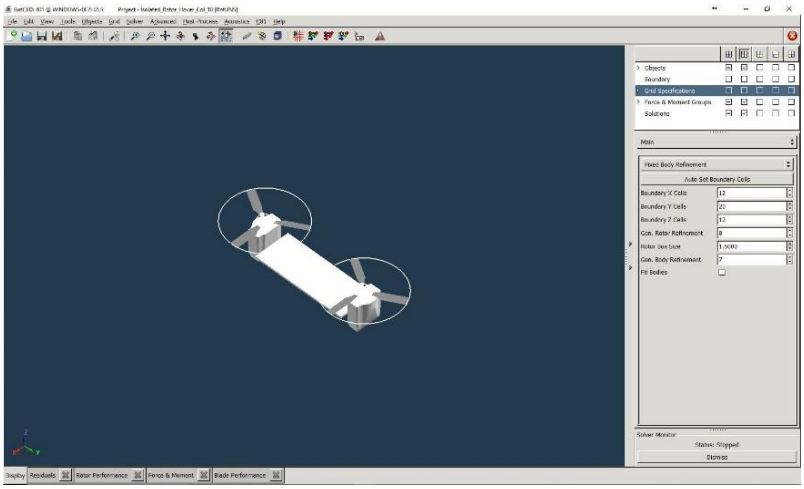

Fig. 3.2. RotCFD GUI with wing/rotor hover flight configuration and simulation set-up features

All dimensions and specifications of a simulation case may be set using the tab window on the right side of the RotCFD GUI main window. The objects menu controls airframe and rotor models. Meanwhile, the boundary menu controls flow properties and type of flight mode to control the overall wall boundary conditions. The grid specification menu controls mesh grid generation options. An example of a boundary condition set-up for flow properties is shown in Fig. 3.3.

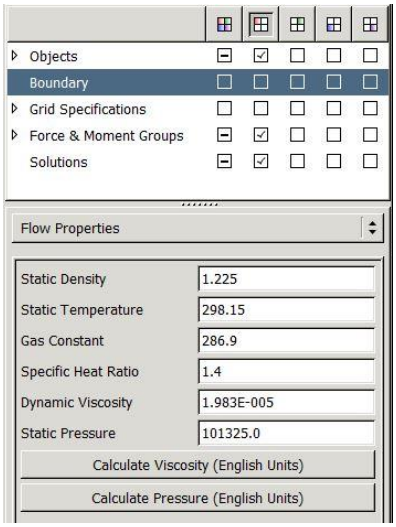

Fig. 3.3. Boundary condition set-up menu for flow properties in RotCFD

Once the rotor's dimensions, flow characteristics, and boundary conditions are defined, a rotor solver method should be selected between steady and unsteady modes. These solvers model the rotor in motion through a momentum change across the rotor area; yet, the interpretation of the source of momentum change is different. The steady solver uses the momentum conservation of the rotor geometry as a disc with aerodynamic loading, as shown in Fig. 3.4 (a). The unsteady solver counts each blade as an individual element in motion, accounting for interactions of flow characteristics, such as the wake vortices produced by a previous blade passing, as shown in Fig. 3.4 (b) [28]. The unsteady solver was used during the current study to understand more realistic flow interactions between the rotors, wing, and pods. It resulted in a higher computing budget for RotCFD, due to the increase in required calculations for each blade element.

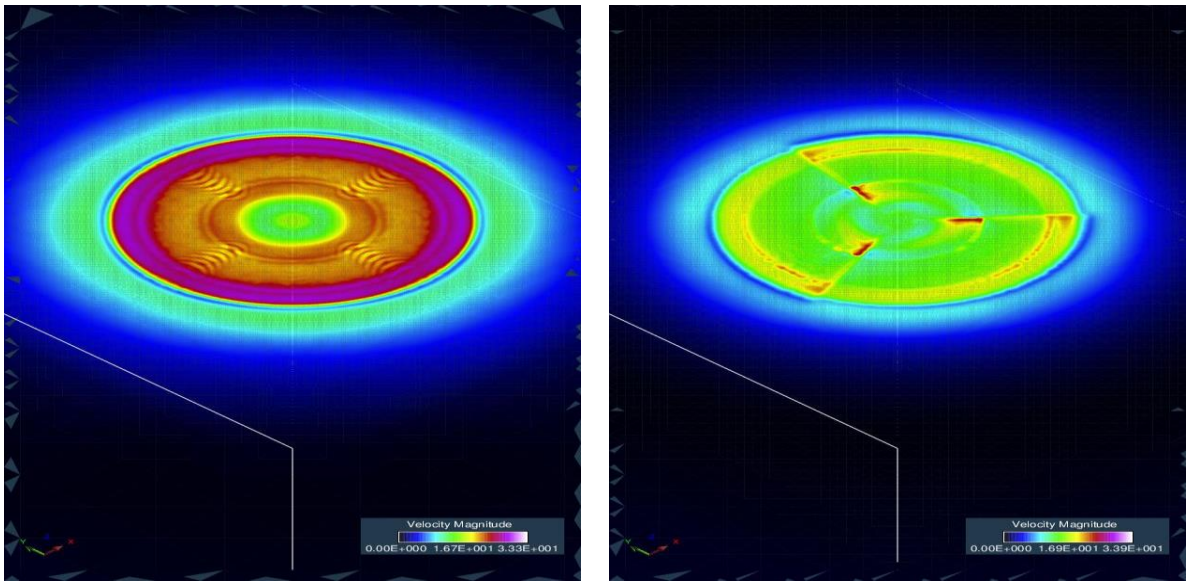

(a) Steady Solver **(b) Unsteady Solver**

Fig. 3.4. RotCFD steady solver and unsteady solver velocity magnitude results comparison [28]

3.3. Configuration of Simulation Cases

For the simulations, the flow properties are defined in Table 3-2. These properties are standard sea level conditions with an ambient temperature of 25°C.

Table 3-2. Flow properties for RotCFD simulation

Gas Properties	Value
Static Density (kg/m^3)	1.225
Static Temperature (K)	298.15
Gas Constant ($J/kg \cdot k$)	286.9
Specific Heat Ratio	1.4
Dynamic Viscosity ($N \cdot s/m^2$)	1.983E-5
Static Pressure (kPa)	101.325

The simulated model consists of two rotors, two pods, and a simple rectangular plate serving as a wing. It closely replicates the experimental configuration discussed in Section 2.1. The RotCFD simulation consists of two rotors with dimensions stated in Table 3-3. These closely replicate the rotor dimensions of KARI's PTUAV. RotCFD allows users to modify the blade's chord length profile. For the current study, these profiles were configured to replicate an actual rotor blade, which was used in both wind tunnel testing and PIV, which was discussed in Section 2.2 and Section 2.3, respectively. The rotor size for the experiment used a 1/8 scale of the computational simulation. The overall configuration of the two different rotors is consistent, as shown in Fig. 3.5 (a) and Fig. 3.5 (b). The airfoil selection was based on the measurement of the actual blades used for experiments, per Section 2.1.

Table 3-3. Rotor dimensions in experimental set-ups and RotCFD simulation

Properties	Experimental		RotCFD	
Radius (m)	0.125		1	
Chord Length (m)	0.025		0.2	
No. of Blades	3		3	
Cone Angle (°)	0		0	
Collective Pitch (°)	0, 5, 10, 15		0, 5, 10, 15	
Cut-Out Radius (m)	0.0251		0.2	
Hinge Offset (m)	0.025		0.2	
Airfoil Profile	NACA0012		NACA0012	
Rotation Direction	Left: CCW	Right: CW	Left: CCW	Right: CW

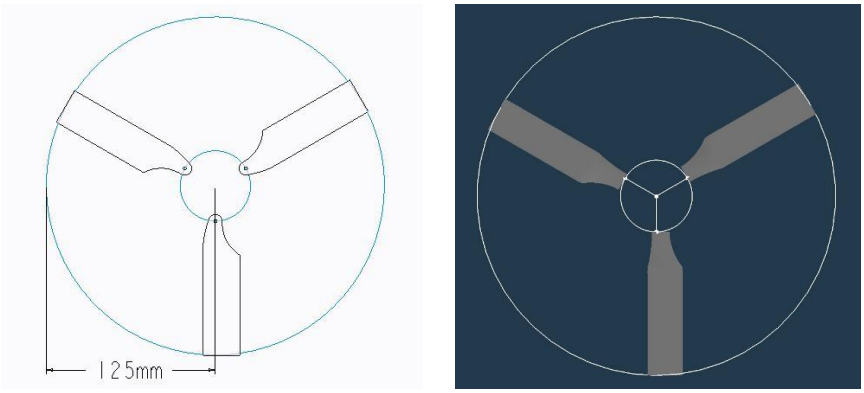

(a) Actual 3D replica of a single rotor **(b) Rotor configuration on RotCFD**

Fig. 3.5. Comparison of rotors in experimental set-ups and RotCFD Simulation

After the two rotors were configured in the simulation, their center locations were adjusted to maintain a distance of exactly 3 rotor radii away from each other, as discussed in Section 1.1. A 3D model of the wing/pods assembly was positioned underneath the rotor, having a wing location of z =-0.575m The configuration is shown with three different views in Fig. 3.6.

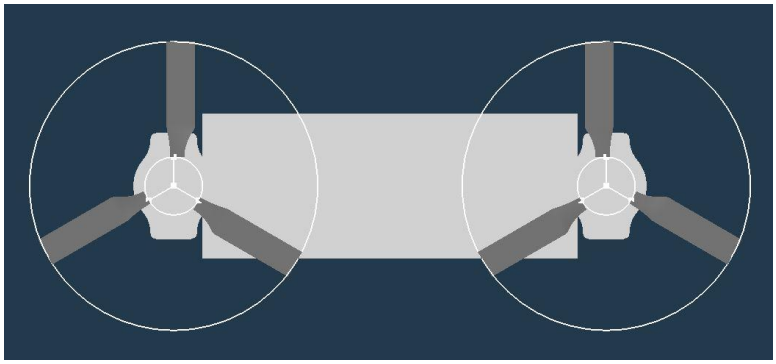

<Top View>

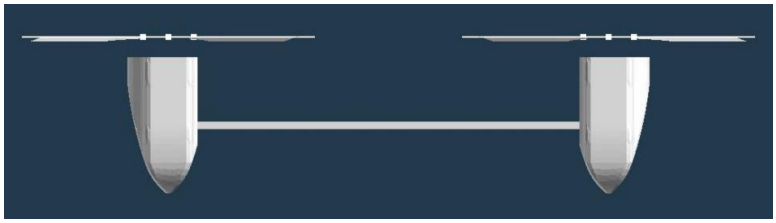

<Front View>

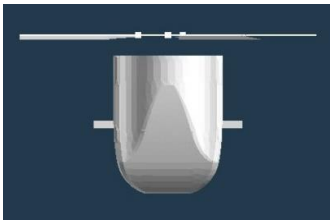

<Side View>

Fig. 3.6. 3D model of wing/rotor configuration in simulation

Wall boundary conditions were set for three different freestream velocities of V_∞ =10,15, and 20m/s These velocities were selected to replicate the wind tunnel test conditions discussed in Section 2.2. An example of these wall boundary conditions for V_∞ =15m/s are defined in Table 3-4.

Table 3-4. Wall boundary conditions specification for V_∞ = 15 m/s

	x-walls		y-walls		z-walls	
	Upper	**Lower**	**Upper**	**Lower**	**Upper**	**Lower**
x-velocity (m/s)	Mass Outflow	15	15	15	15	15
y-velocity (m/s)	0	0	0	0	0	0
z-velocity (m/s)	0	0	0	0	0	0

3.4. Grid Generation and Convergence Test

RotCFD's grid generation uses an unstructured 3D Cartesian Octree meshing scheme. A 3D Cartesian Octree grid scheme uses one cubic cell divided into 8 smaller cubic cells as the refinement degree increases. In each RotCFD simulation case, the mesh generation was controlled in order to maintain finer grids near the body and rotors. This meshing scheme simplifies the mesh cell generation process. Also, it constitutes RotCFD as a user-friendly program. The RotCFD mesh grid generation results for the body and rotor are shown in .

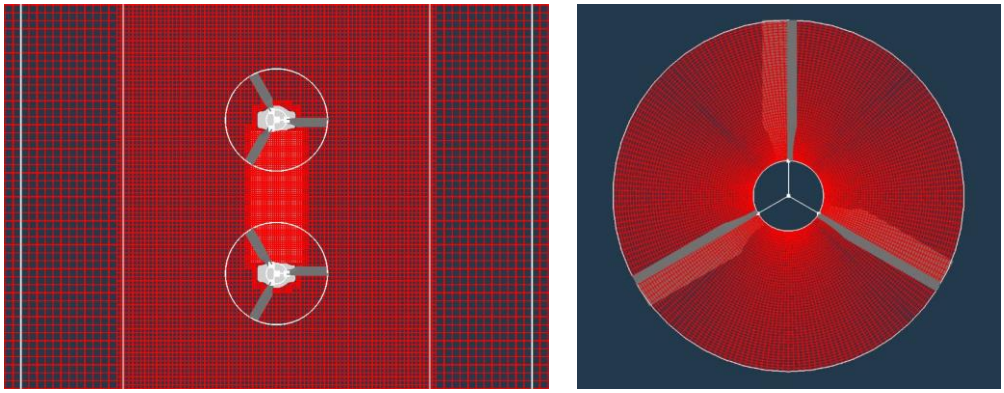

(a) Octree grid mesh generation scheme result **(b) Rotor disc radial grid result**

Fig. 3.7. Octree grid mesh in RotCFD simulation and radial grid for rotor disc

To ensure consistency of the simulation results, a convergence study was completed with 5 different grid specifications, as shown in . The grid refinement level indicates how many times grid cell division processes was performed on one cubic cell for each refinement box specified, near the 3D body, and rotor, as shown in .

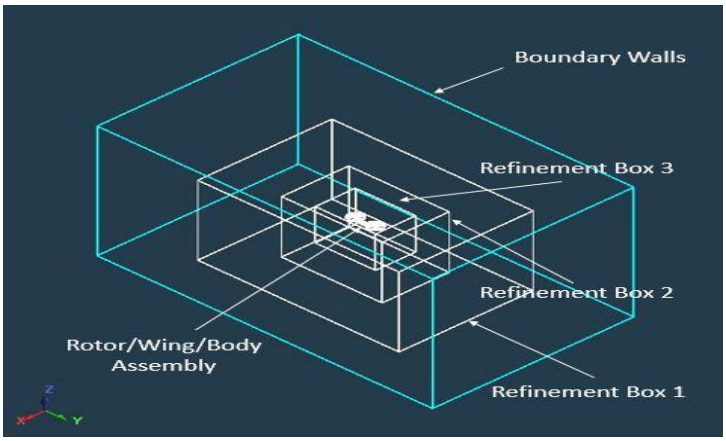

Fig. 3.8. Grid cell refinement volume designation

A higher refinement degree generates more grid cells in the meshing process. However, the computation time required for one case to converge increases. The outcome of the convergence test for thrust coefficient C_T is shown in .

Table 3-5. Grid convergence test specification of cases

Grid refinement degree	Coarsest	Coarser	Fine	Finer	Finest
Refinement Box 1	1	2	3	5	5
Refinement Box 2	2	3	4	6	6
Refinement Box 3	3	4	5	7	7
3D body grid refinement level	4	5	6	7	8
Rotor grid refinement level	5	6	7	8	9
Number of grid cells	58,588	337,532	2,169,168	7,675,984	15,312,756
Convergence time length	1 hr	10 hrs	4 days	10 days	21 days

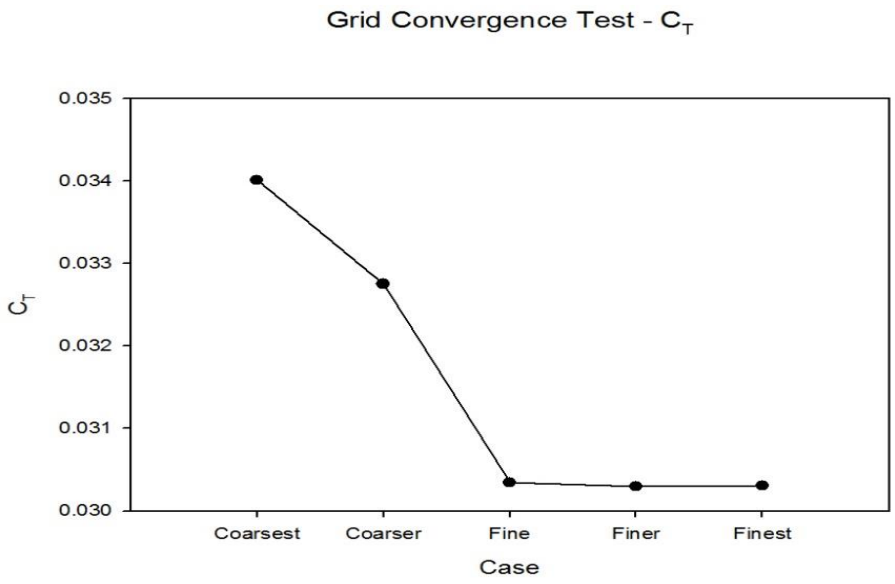

Fig. 3.9. Convergence test for thrust coefficient in RotCFD

As observed in Fig. 3.9, the outcome of the simulation does not change significantly between the two cases with finer grid meshing and with the finest grid meshing. Meanwhile, the computation time required for the case to converge is nearly twice for the finest grid meshing case. Therefore, the simulations performed in the current study were conducted with the finer mesh.

Chapter 4

Results and Discussion

The previous chapter discussed two different types of experimental methods used to investigate the fountain effect of a tiltrotor's wing/rotor configuration and also discussed a validation of the RotCFD simulations. First, a series of experiments were conducted for a basic hover flight condition using a wing/rotor configuration test rig. In addition to the thrust measurement of two rotors, PIV data acquisition was conducted to observe the flow characteristics on the wing surface. For purposes of validation, a visualization of the PIV results was then compared to RotCFD's flow visualization data. Second, a wing/rotor configuration was tested in the subsonic wind tunnel. The purpose of the wind tunnel test was to replicate crosswind conditions with different freestream velocities and crosswind angles.

4.1. Hover Flight Condition Test Results

4.1.1. Wing/Rotor Performance Comparison from Experiments and CFD Simulations

Performance of the tiltrotor wing/rotor configuration in hover was tested using an experimental set-up and RotCFD simulations. Comparisons of the experimental result and the computational result aimed to investigate how closely they replicate each other. This effort facilitated a greater understanding of the validity and limitations of the computational simulations.

First, the thrust performance of the two rotors was acquired, using the wing/rotor configuration test rig. Preliminary thrust measurement of each rotor demonstrated that higher download drag occurred when both rotors were operated compared to when either side of the rotor was operated independently. An additional download drag was observed. The total thrust was measured from the load cells installed in the test rig, as shown in Table 4-1. This measurement confirmed the download influence of the fountain effect, causing a decrease to the rotor performance of the wing/rotor configuration.

Table 4-1. Rotor total thrust comparison for two different operation modes

Blade Pitch Angle (°)	**Total Thrust (N)**		**Additional Download**
	Individual	Simultaneous	
5	1.8929	1.7793	6%
10	3.7622	3.5593	5.7%
15	5.6926	5.2856	7.7%

Second, thrust forces from each rotor and download drag were calculated from the RotCFD simulations. The purpose of these simulations was to obtain the total thrust from each case of varying freestream conditions and different blade pitch angles. To ensure validity for each simulation case, the CFD convergence was determined using the mass residual value recorded along the time steps, as shown in Fig. 4.1. When the mass residual plot converges into a steady state with minimal variations, it was assumed that the case was converged.

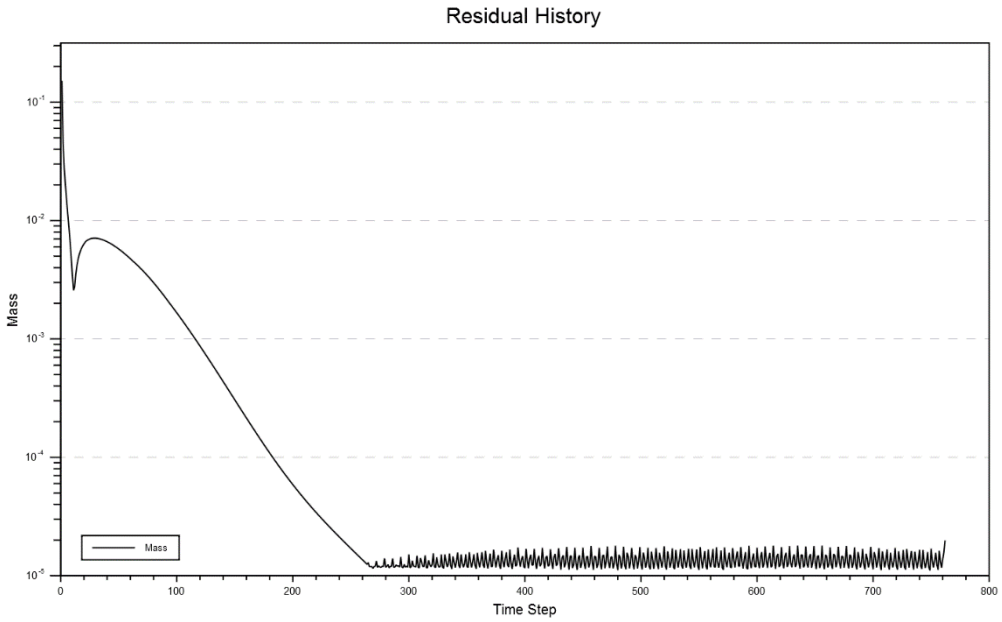

Fig. 4.1. RotCFD simulation case mass residual plot

To calculate the overall thrust of the rotor/wing configuration simulated in RotCFD, three different force components were taken and combined. RotCFD focused on obtaining the thrust of each individual rotor and the download drag force exerted on the wing/body model. The total thrust, T_{total}, was calculated using the following equation,

$$T_{total} = T_{right} + T_{left} - D_{download} \quad \textbf{(4.1)}$$

where, T_{right} is the thrust from the right rotor, T_{left} is the thrust from the left rotor, and $D_{download}$ is the download drag. Due to the nature of URANS CFD codes, RotCFD's blade element simulation provides an unsteady rotor thrust as a function of the time step. Consequently, the mean thrust was calculated by averaging thrust values across time. This started with a time step, where the thrust was converged, and it ended with a final time step, as shown in Fig. 4.2. A download force was evaluated using the same approach: by averaging drag over time steps after the solution converged, as shown in Fig. 4.3.

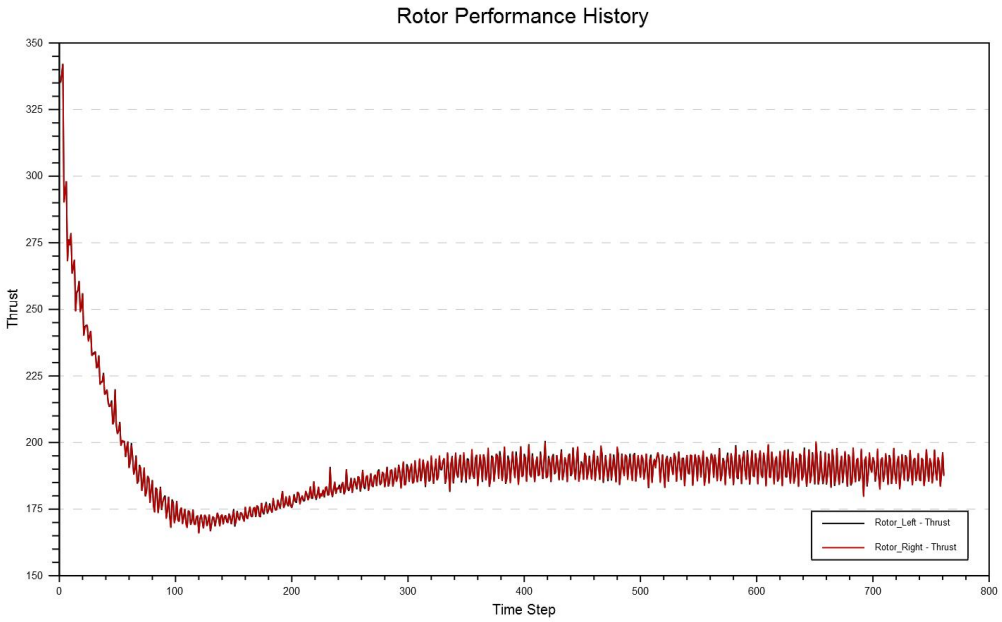

Fig. 4.2. RotCFD simulation case thrust measurement plot for two rotors

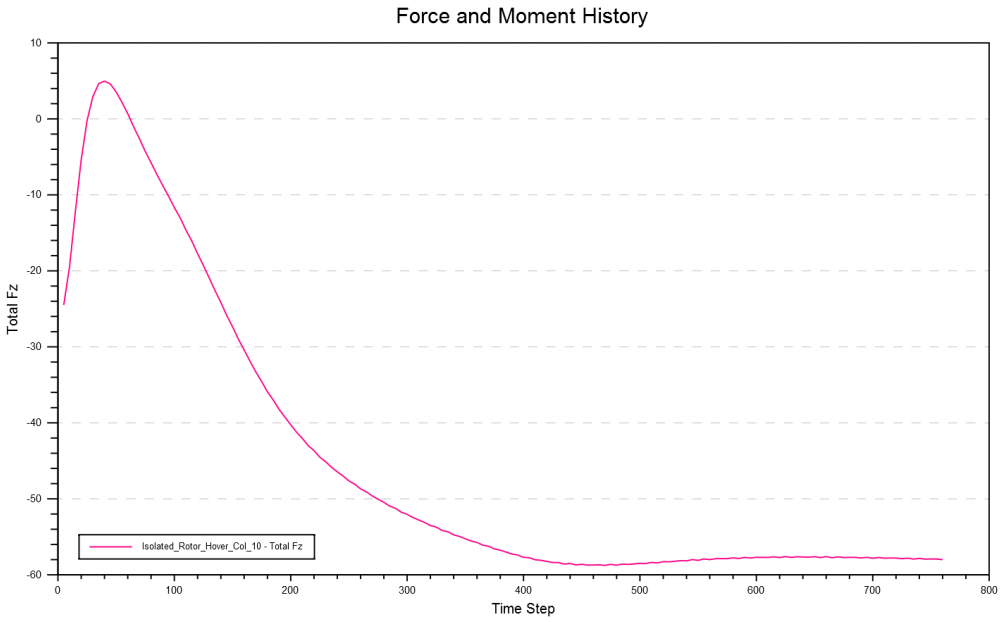

Fig. 4.3. RotCFD simulation case download drag plot on wing structure

Then, the calculated total thrust from the RotCFD simulation was non-dimensionalized, using Eq.(2.1 and the prescribed-flow conditions per Table 3-2. Comparisons of the non-dimensionalized thrust coefficient were performed between the experimental and computational

data. Such comparisons revealed that the RotCFD simulations closely represented the performance of the wing/rotor configuration in an experimental set-up for all blade pitch angles, as shown in Fig. 4.4. This result indicates that the RotCFD simulation can represent hover flight for the tiltrotor's wing/rotor configuration. It demonstrates a trend whereby rotor thrust increases linearly as blade pitch angles increase for a region of 5° to 15°. Also, it was observed that a RotCFD simulation produced using isolated rotors with an actuated disk method demonstrates thrust increase in a linear manner, but with a different slope. This observation suggests that the fountain effect's influence on a wing/rotor configuration may increase as the blade pitch angle increases.

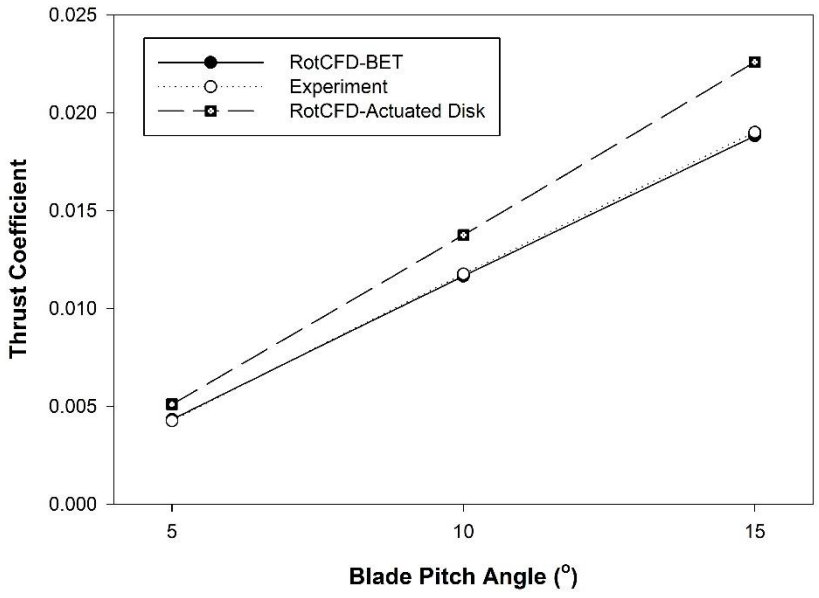

Fig. 4.4. Thrust coefficient comparison of experiment and RotCFD simulation results for hover condition

4.1.2. Flow Visualization of PIV and RotCFD Results Compared

To investigate flow characteristics associated with the fountain effect, PIV experiments were performed. From each pair of images, it was observed that the fountain effect that occurs on the wing structure is highly turbulent, shifting its center between right and left pod locations. A post-processing minimum of 300 image pairs for two different pitch angles of 5° and 10° demonstrates an average velocity magnitude of the fountain effect. This is compared to RotCFD velocity magnitude contours, shown in Fig. 4.5 and Fig. 4.6. The area of PIV testing, where two rotors were visible, was blocked when acquiring PIV images to prevent laser reflections of the rotors from damaging the camera. In Fig. 4.5 and Fig. 4.6, this region has been masked with a white rectangular section. Due to the blocked area on two rotors, the high-speed flow—observed at the suction on top of the rotors (shown by RotCFD visualization)—is not clearly visible in the PIV results.

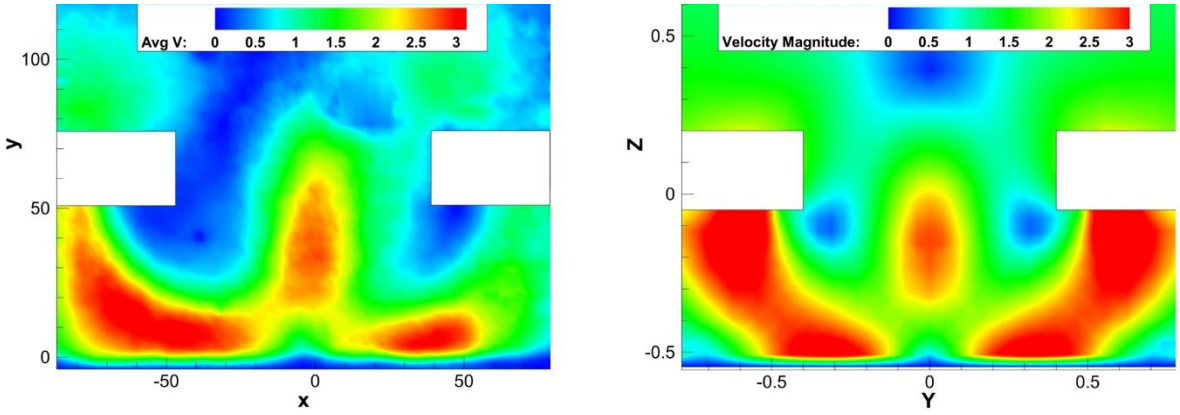

Fig. 4.5. Comparison of RotCFD and PIV visualization results of fountain effect (θ = 5°)

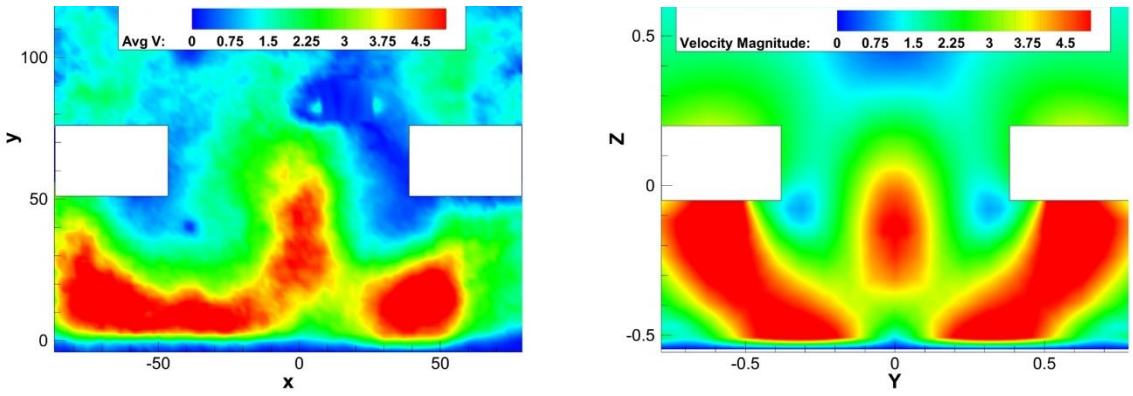

Fig. 4.6. Comparison of RotCFD and PIV visualization results of fountain effect ($\theta = 10°$)

Clearly, these results indicate how RotCFD can simulate fountain effect's flow characteristics, which are close to the averaged PIV visualization. One downside of RotCFD is that it is impossible to duplicate the turbulence of the fountain effect exactly how it occurs during real experiments. Consequently, RotCFD may be useful for measuring the magnitude of the fountain effect's overall flow structure and its influence on a simple wing/rotor model. It may not be useful, however, for measuring turbulence flow characteristics.

4.2. Forward Flight and Crosswind Flight Conditions Test Results

After investigating the performance of the wing/rotor configuration under a hover flight condition (Section 4.1), a series of forward flight and crosswind flight condition tests were performed in a sub-sonic wind tunnel. Additionally, a series of RotCFD simulations was performed. At high crosswind angles, it was predicted that the RotCFD simulations and experimental measurements would have limited agreement. This lack of agreement would be attributed to the limitation of URANS CFD codes for predicting highly separated and turbulent flows in high crosswind angle conditions. This assumption proved true for both the fixed freestream velocity test and the fixed blade pitch angle tests.

4.2.1. Thrust Coefficient with Fixed Freestream Velocity

Fig. 4.7 demonstrates the non-dimensionalized thrust coefficients resulting from the experiment and the RotCFD simulations for three different blade pitch angles at a fixed freestream velocity of $V_\infty = 15\text{m/s}$. A comparison of the thrust coefficients—between the experiment and simulations—clearly demonstrates a discrepancy for high crosswind angles at $\beta = 75°$ and $90°$. For both pitch angles, RotCFD overestimates thrust performance of the tiltrotor's wing/rotor configuration at high angles of crosswind, indicating that the suggested limitation of RotCFD is valid. For low angles of crosswind, ranging from 0-60°, the RotCFD simulations closely follow the quantitative trend from the experimental results. This observation indicates that RotCFD is capable of replicating low crosswind angle flight conditions.

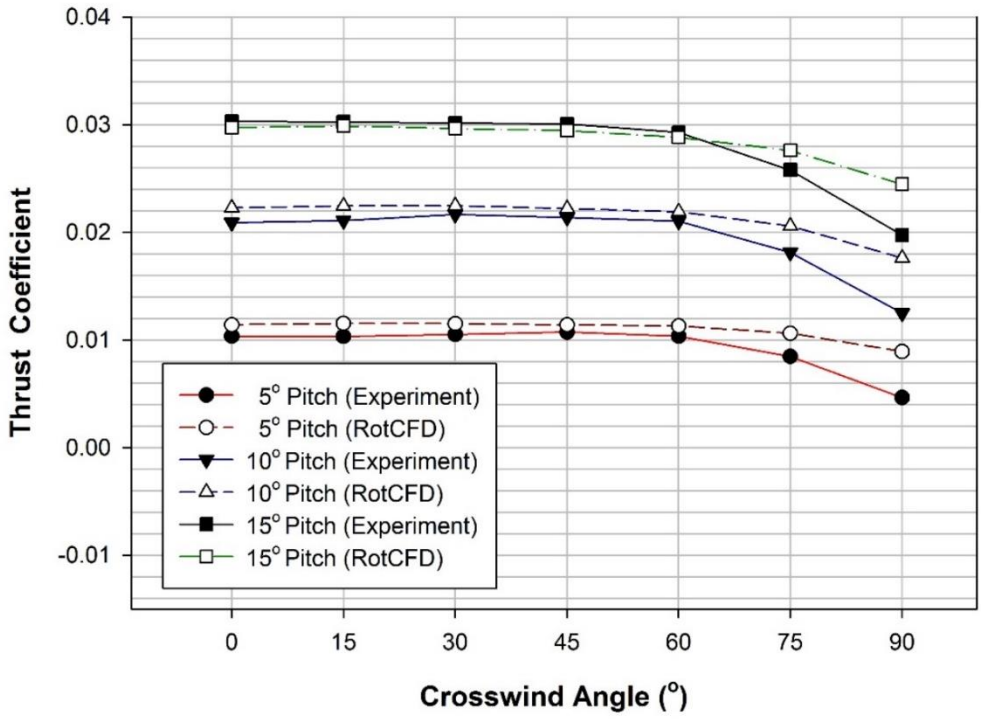

Fig. 4.7. Thrust coefficient comparison for different crosswind angles at $V_\infty = 15$ m/s with $\theta = 5°$, 10°, and 15°

A total of four cases were simulated for the one-eighth scaled model, with one case of the hover flight condition at a blade pitch angle of $\theta = 15°$, and three cases for crosswind conditions with a freestream velocity of $V_\infty = 15$ m/s and crosswind angles of $\beta = 0°$, 45°, and 90°. A comparison of the thrust coefficients further confirmed the limitations of the RotCFD solver in regards to highly separated and turbulent flows for the high crosswind angle $\beta = 90°$. The result for the scaled simulations also demonstrated a decrease of the overall aerodynamic performance of the rotors in comparison to the full-scale simulations. The overall trend in the thrust performance in lower crosswind angles was consistent for both full-scale simulations and scaled simulations, as shown in Fig. 4.8.

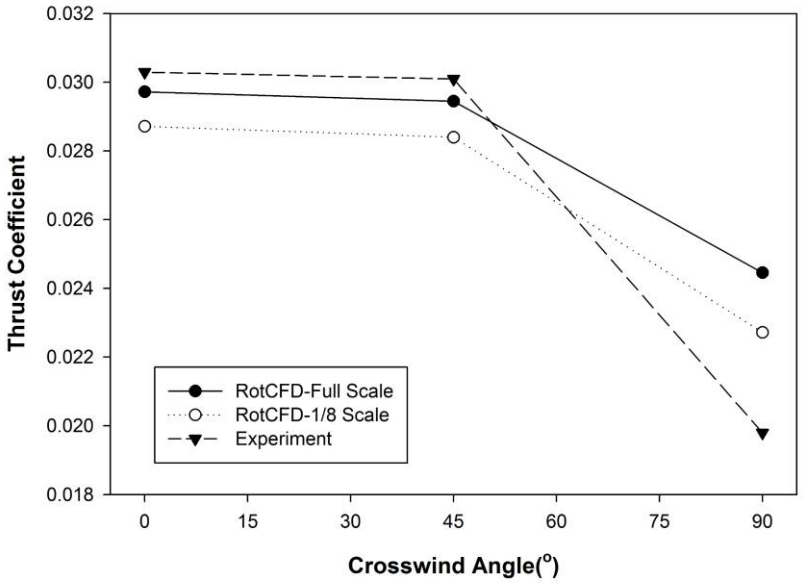

Fig. 4.8. Thrust coefficients comparison of the sub-scale and the full-scale RotCFD simulations and the experiment results

A comparison of the cross-flow velocity for the full-scale and sub-scale simulations was also conducted, as shown in Fig. 4.8. These results were obtained for a hover flight condition and a blade pitch angle of $\theta = 15°$, along with crosswind flight conditions at a freestream velocity of

V_∞ =15 m/s and crosswind angles of $\beta = 0°$ and 45°. The fountain effect structures for both the scaled simulation and full-scale simulation were nearly identical to each other with only a slight difference in velocity of the flow induced by the rotors. The overall flow separation structure observed for the crosswind flight conditions of $\beta = 0°$ and 45° for both the scaled simulations and the full-scale simulations also replicated each other closely.

<Sub-Scale>

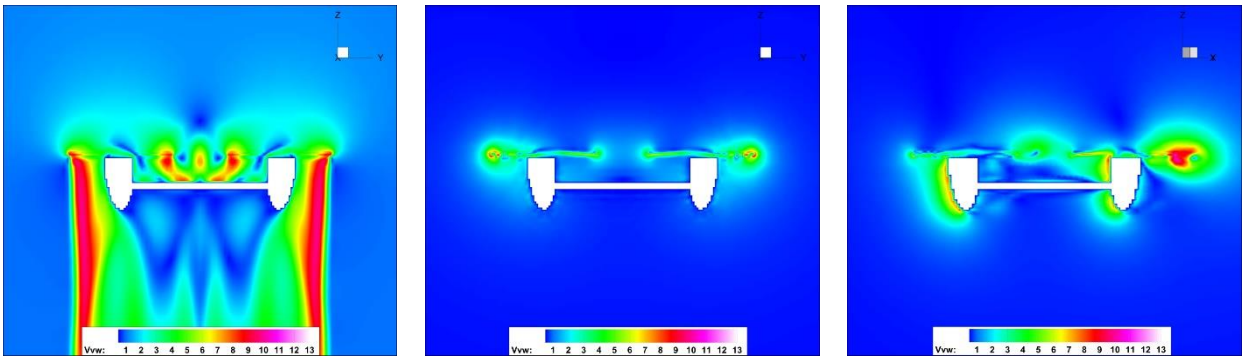

<V_∞= 0 m/s, $\beta = 0°$ > **<V_∞= 15 m/s, $\beta = 0°$>** **<V_∞= 15 m/s, $\beta = 45°$>**

<Full-Scale>

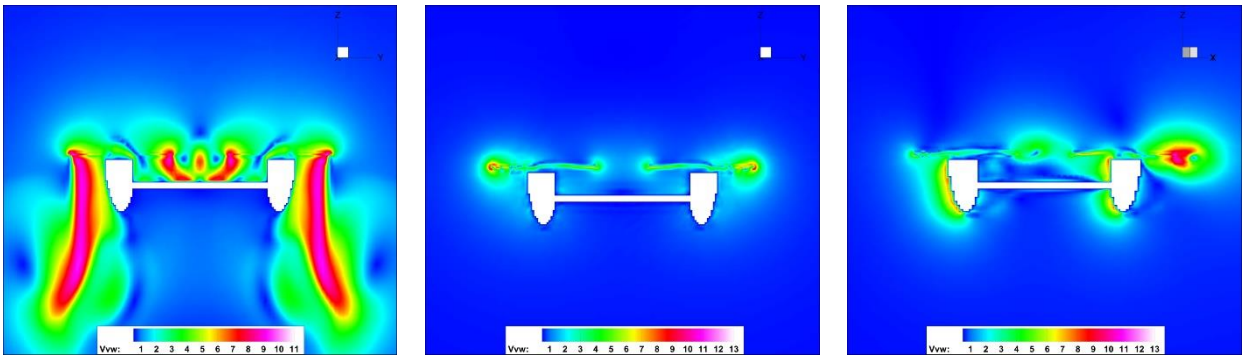

<V_∞= 0 m/s, $\beta = 0°$> **<V_∞= 15 m/s, $\beta = 0°$>** **<V_∞= 15 m/s, $\beta = 45°$>**

Fig. 4.9. Velocity magnitude contour of the sub-scale and the full-scale RotCFD simulations of a hover flight and crosswind flight conditions at a blade pitch angle of $\theta = 15°$

4.2.2. Thrust Coefficient with Fixed Blade Pitch Angle

The thrust coefficients for the wing/rotor configuration across four different freestream velocity conditions and a fixed blade pitch angle of 15° were compared, as shown in Fig. 4.10. RotCFD simulation results and experiment results closely match for V_∞ = 0 and 10m/s. However, results for V_∞ = 15m/s and 20m/s indicate that RotCFD underestimates wing/rotor performance compared to experiment results. This discrepancy increases for higher freestream velocity conditions, V_∞ = 20m/s. Nevertheless, the overall trends of the thrust coefficient results agree, between the experiment and RotCFD. This observation indicates that RotCFD can reasonably predict forward flight condition performance.

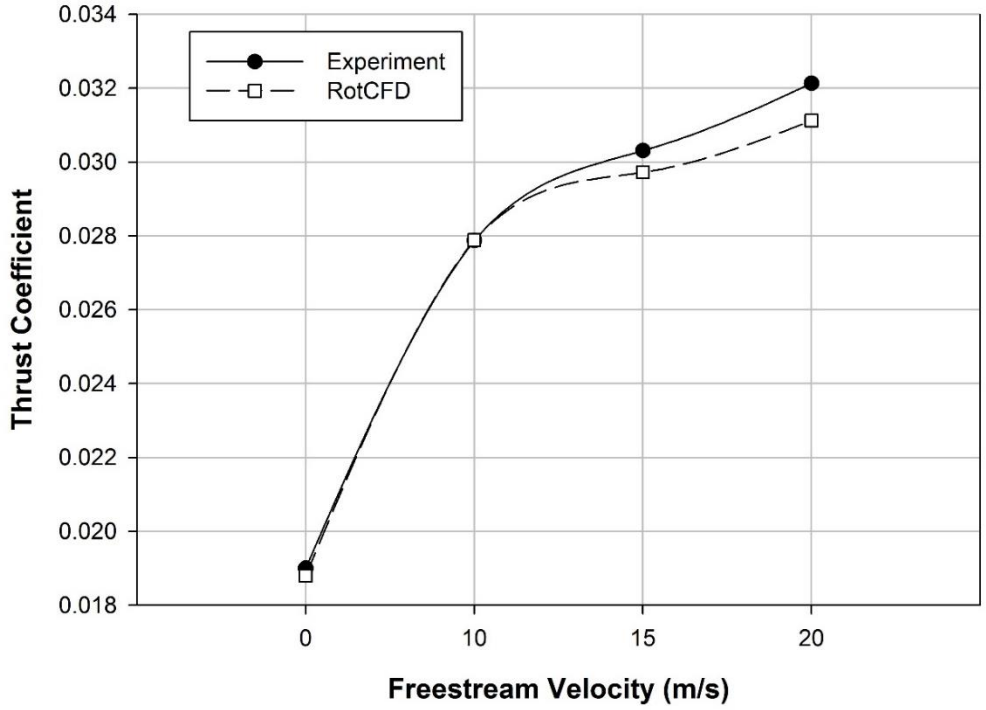

Fig. 4.10. Thrust coefficient comparison for forward flight condition in V_∞ = 10, 15, and 20 m/s at θ = 15°

Providing further freestream velocity conditions with crosswind demonstrates that the experimental results and the RotCFD simulation results agree at lower crosswind angle

conditions. Nevertheless, there is great discrepancy between experiment results and RotCFD simulations for high crosswind angles, as shown in Fig. 4.11. An overall trend of this fixed blade pitch angle test result presents the following differences in comparison to a fixed freestream velocity condition test of V_∞=15m/s. For a fixed blade pitch angle test, an experiment result demonstrates a thrust coefficient drop at a crosswind angle of 60°. Meanwhile, a fixed freestream velocity test demonstrates a thrust coefficient drop at a crosswind angle of 75°. For RotCFD simulations, when using a fixed blade pitch angle, demonstrated that a thrust coefficient drop occurs at the crosswind angle of 60° for V_∞= 10m/s, at 75° for V_∞= 15m/s, and at 90° for V_∞= 20m/s. This trend suggests that the flow separation behind the wing and pods is more dominant for lower freestream velocity conditions. Thus, when crosswind angles are lower, the thrust performance decreases at lower freestream velocities.

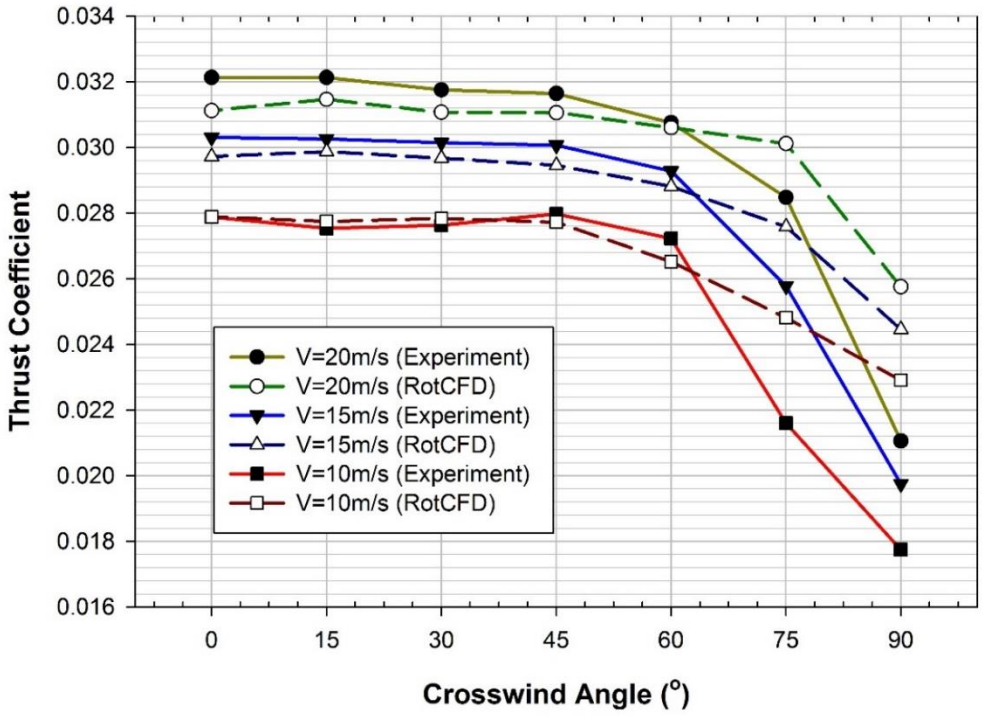

Fig. 4.11. Thrust coefficient comparison of wind tunnel experiment results and RotCFD simulations (θ = 15°)

In general, the simulations performed in this study suggest that RotCFD simulation could predict wing/rotor performance at lower crosswind angles, ranging from 0° to 45°. A major cause of discrepancy at higher crosswind angles' flight conditions—between experiment and RotCFD simulations—was due to limitations of the URANS CFD methodology, as previously acknowledged. Therefore, the flow field characterization of the fountain effect from RotCFD simulations is limited to low crosswind angle flight conditions. These are used to provide an understanding of how crosswind would affect the performance of the tiltrotor's wing/rotor configuration.

4.3. Visualization of Flow Characteristics of RotCFD Simulations

Section 4.1 discussed a fountain effect structure visualization of the RotCFD simulation and PIV experiment. The result indicated that RotCFD could replicate an overall structure of the fountain effect flow structure, which occurs on a wing/rotor configuration's wing surface. Further, Section 4.2 discussed RotCFD's capability of predicting flow characteristics for lower crosswind angle flight conditions at $\beta = 0°$, 15°, 30°, and 45°. Moreover, these sections indicated that RotCFD simulation flow visualization results might be helpful for understanding the flow interactions of wing/rotor configuration and influence of crosswind flight conditions on performance.

4.3.1. RotCFD Flow Visualization of Forward Flight Conditions

The first flow visualization comparison was performed with a zero-crosswind angle at different freestream velocities. Clearly, the fountain effect is present on the wing surface for V_∞ = 0m/s. Then, it immediately diminishes under a non-zero freestream condition in the simulation, as shown in Fig. 4.12. This observation indicates that a forward flight condition for the tiltrotor

aircraft diminishes the fountain effect. Moreover, the additional download effect will be eliminated. Also, the rotor tip vortex region decreases as freestream velocity increases. This trend confirms the increase of a rotorcraft's performance in forward flight in comparison to a hovering flight. A decreased rotor tip vortex is known to cause higher rotor performance, which is referred to as translational lift [29].

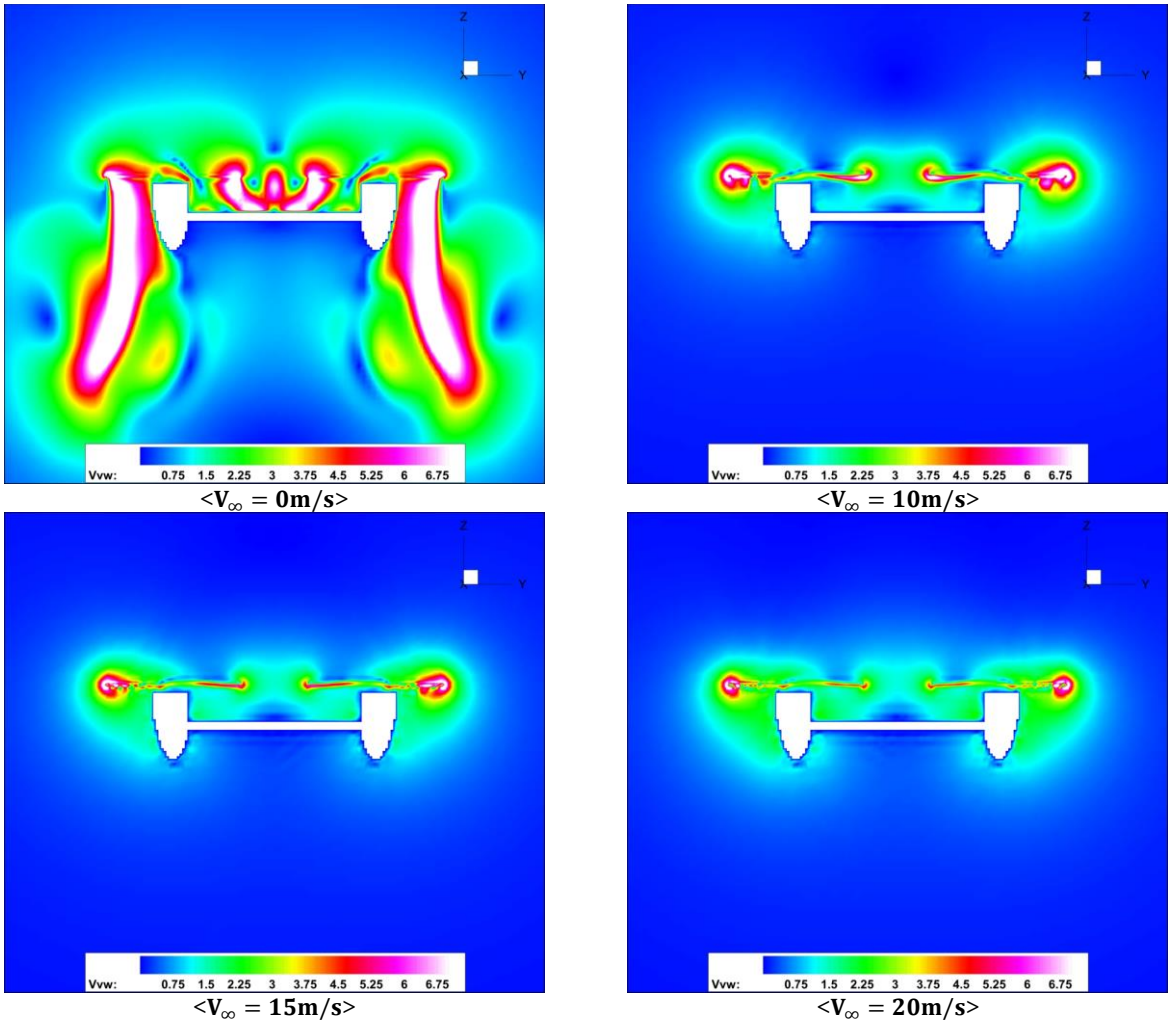

Fig. 4.12. Velocity magnitude contour comparison for different freestream velocity conditions ($\theta = 15°$)

A comparison of velocity magnitude iso-surface results from the simulations was also performed to visualize the influence of the freestream on the flow structure in 3-dimensional space. It can be observed that the fountain effect is diminished with the addition of a freestream

flow. Moreover, the rotor's tip vortex decreases, as shown in Fig. 4.13. From the hover condition to the freestream condition of V_∞=10m/s, a size of the flow reduction for both fountain effect and rotor tip vorticity is largest. Fig. 4.10 indicates thrust coefficient jump. Then, the rotor tip vorticity decreases its size as the freestream velocity increases, though this subsequent increase in thrust is not as large as that produced between the hover flight and the flight condition of V_∞=10m/s, which is also indicated.

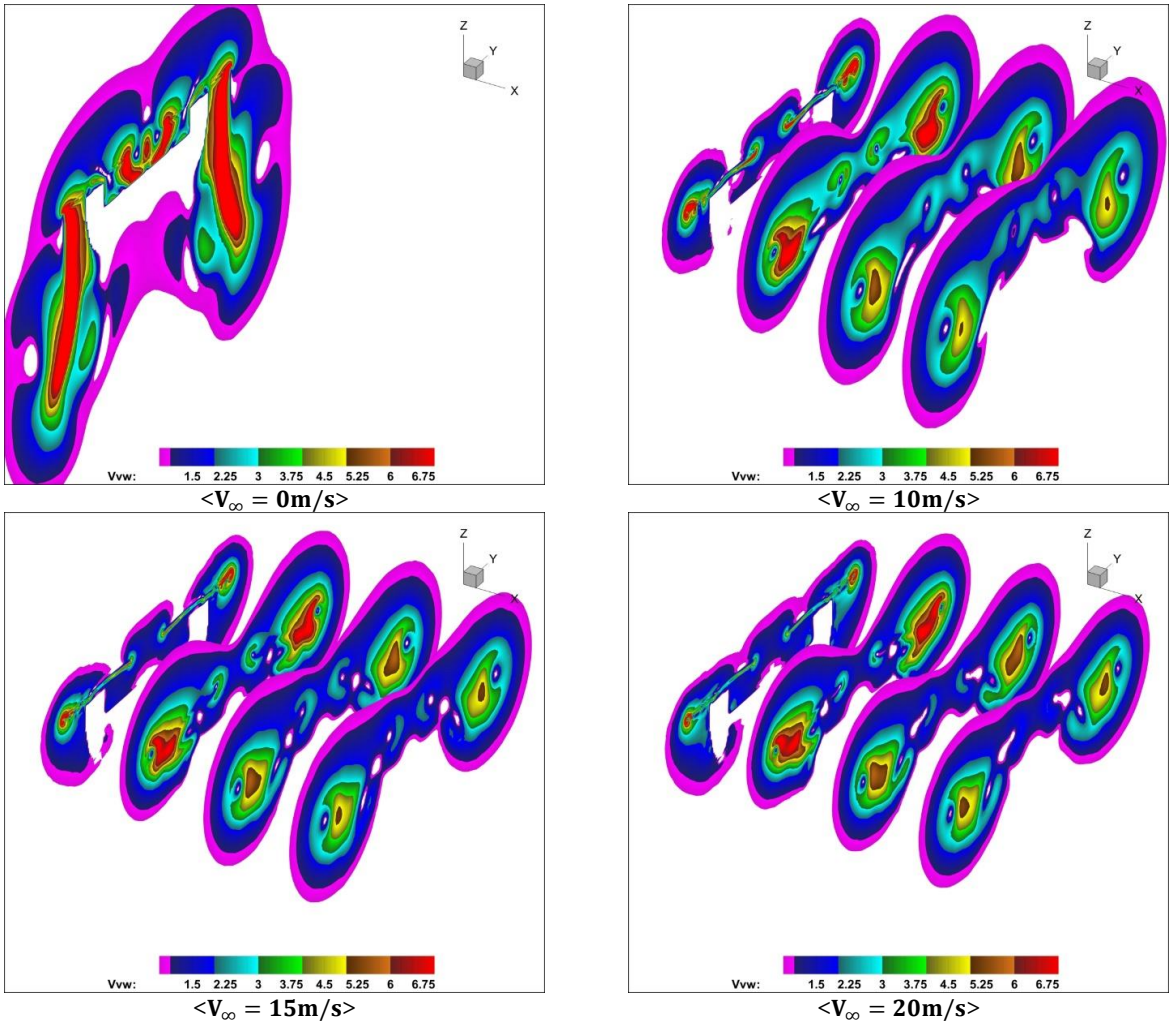

Fig. 4.13. Flow iso-slice visualizations of forward flight condition in V_∞ = 0, 10, 15, 20m/s

4.3.2. RotCFD Flow Visualization of Crosswind Flight Conditions

A comparison was also performed for the flow field of the wing/rotor configuration at different crosswind angles. As discussed in Section 4.2, only crosswind angles up to 45° were compared, since RotCFD's predictions of higher crosswind angle conditions demonstrated disagreement with the experimental results. Fig. 4.14 illustrates 2-dimensional velocity magnitude contours across the middle of the wing/rotor with the blade pitch angle of $\theta = 15°$ for 4 different angles of $\beta = 0°$, $15°$, $30°$, and $45°$.

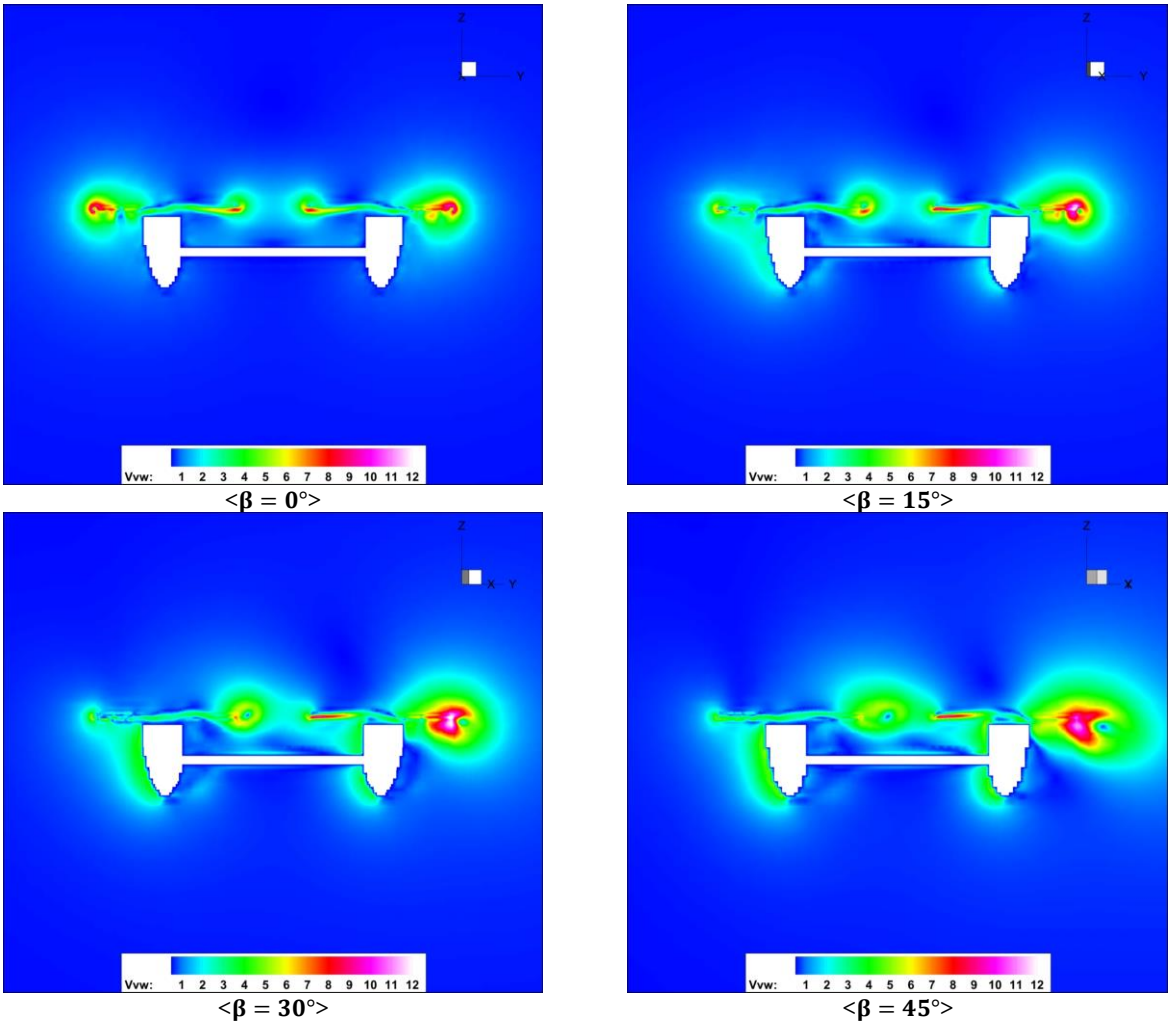

Fig. 4.14. Flow velocity magnitude contours for different crosswind angles in $V_\infty = 10$ m/s and $\theta = 15°$

The result indicates that the fountain effect flow structure is diminished with the addition of a freestream component, as previously observed in the forward flight flow visualizations. Notably, however, a rotor tip vorticity presents again, and its magnitude increases as the crosswind angle increases. Further, a low speed flow underneath the right rotor occurs. Its overall magnitude and size increases as the crosswind angle increases, and the structure of this low-speed flow region is quite different from the fountain effect. Nevertheless, the induced flow beneath the left rotor is fed back into the top of the rotor, demonstrating a momentum flow change reflected from the wing structure.

Observations from Fig. 4.14 indicate that higher crosswind angle flight conditions might influence wing/rotor configuration performance in a similar way to the fountain effect during a hover flight condition, resulting in download increase. In addition to the tip vortex size increase, flow visualization results for crosswind flight conditions produce a performance decrease of the wing/rotor configuration, relative to a 0° freestream.

Chapter 5

Conclusion

5.1. Summary

This study employed computational simulation and experimental methodologies to investigate the aerodynamic performance and flow interactions of a tiltrotor's wing/rotor configuration. This study's scope covered the hover-flight condition and crosswind flight condition for a tiltrotor aircraft. The fountain effect is one of the most commonly recognized causes of additional download drag and a tiltrotor aircraft's performance inefficiency, which occurs during hover flight. This effect was the study's primary object of investigation. Understanding the crosswind flight condition's effects on the fountain effect constituted another focal point of this study. To achieve these objectives, two sets of experimental test sequences were designed. Further, a CFD simulation tool was used for comparison to these experiments. A URANS-based code was used on account of its low computing budget, despite its limitations for solving complex turbulent flow, which may persist in a simulated region. DNS and LES codes were considered in this study. They were eliminated, however, due to the demanding computation power required for both types of solvers.

A tiltrotor's wing/rotor configuration model was designed to replicate a typical tiltrotor's wing, engine pods, and rotors, which are major components of the testing subject. For a hover flight condition, the wing/rotor configuration model was fixed on an optics table to measure the performance of two rotors. To visualize the fountain effect's flow structure, which occurred on

the wing, a PIV experiment was performed. For the crosswind flight condition, the wing/rotor configuration model was installed in the test section of the 3x4ft low speed wind tunnel at UIUC Aerodynamics Research Laboratory. The test section included a rotational plate that allowed for the model to change its angle relative to the freestream inside of the wind tunnel, replicating different crosswind angles. The first sequence of the wind tunnel test involved three different freestream velocity conditions V_∞= 10, 15, and 20m/s with a fixed blade pitch angle $\theta = 15°$. The second sequence of the wind tunnel test was followed by three different blade pitch angles $\theta = 5°$, 10°, and 15° with a fixed freestream velocity V_∞= 15m/s. The thrust value for each condition was acquired through a LabView VI program's data acquisition system, post-processed, and non-dimensionalized to calculate thrust coefficient as the wing/rotor model's performance indicator. The rotorcraft-specific URANS Solver, RotCFD, was used to simulate a wing/rotor model in hover flight condition and crosswind flight conditions. Boundary conditions and parameter designs of CFD simulations were identical to the experimental test configuration in order to compare thrust coefficients. Comparisons of the experimental result and the computational result for a hover flight condition presented consistency between the experiments and simulations. PIV visualization results and post-processed CFD flow field visualizations also indicate close representations of each other as regards the fountain effect's flow characteristics.

Moreover, comparison of the experimental result and the computation result for a crosswind flight condition presented agreement for a certain range of crosswind angles. Meanwhile, limitations on the computational simulation method became apparent for the flight condition of extreme crosswind angles. This comparison indicates advantages and limitations of the URANS-based CFD solver. The test conditions, in which the experimental result and the computational result agreed, were carefully determined. The relevant CFD data was post-

processed for flow field visualization to understand how the crosswind flight condition affected the fountain effect, relative to the hover flight condition.

5.2. Conclusion

The following conclusions were established by this study:

1. URANS-based RotCFD solver reasonably simulates the hover flight performance of a tiltrotor's wing/rotor configuration. Thrust coefficients for different blade pitch angles are calculated and compared to the experimental result, showing minimal deviation between CFD and experimental results. Therefore, it can be stated that CFD results and experimental results for a hover flight condition correspond to each other closely for the blade pitch angles of 5° to 15°.
2. Visualization of a fountain effect on the wing surface of a wing/rotor configuration was performed using PIV. Then, the visualization result of PIV was compared to the flow visualization result of RotCFD. The fountain effect for blade pitch angles of 5° and 10° is clearly present for both PIV and CFD results. The structures of the flow characteristics are similar between the experiment and simulation.
3. A series of wind tunnel tests was performed to replicate the crosswind flight condition of a tiltrotor's wing/rotor configuration. Crosswind flight conditions were varied, using different V_∞, θ, and β. Lift coefficients of the wind tunnel tests and CFD results closely replicate each other's results for crosswind angles lower than 60°. Therefore, it can be stated that the URANS-based CFD methodology can simulate the tiltrotor's wing/rotor configuration performance for flight conditions of lower crosswind angles, ideally from 0° to 45° for this particular study.

4. The RotCFD results were post-processed to perform flow visualizations for crosswind flight conditions of lower crosswind angles. A fountain effect is present in the hover flight condition. The effect diminishes in the freestream flight condition. No significant change for thrust coefficient occurs. An induced flow beneath the rotor on the downstream side was observed to occur. Consequently, the thrust coefficient drops, indicating a performance decrease in higher crosswind angles.

5.3. Recommendations

The author would recommend the following for possible future research opportunities to investigate a tiltrotor's wing/rotor configuration performance. For crosswind angles that were higher than 60°, CFD results overestimate lift coefficients in comparison to experimental results. This deviation is expected due to limitations of the URANS-based CFD solver not being capable of simulating complex turbulent flows that might occur behind the engine pod structure in high crosswind angle flight conditions. To understand these complex turbulent flow structures, an LES solver for CFD should be used for results that are more accurate. A DNS solver is another possibility, but its demanding computational budget limits a DNS solver's simulated flow field for low Re numbers, which is not suitable for a rotor-specific CFD simulation.

For a wing/rotor model designed for testing, the wing structure of this study could be designed to have an airfoil cross section to closely replicate the actual tiltrotor aircraft's wing/rotor configuration. To utilize a simple structure that could be tested both in a wind tunnel and on an optics table with PIV experiment, the wing structure for this study was made with a flat plexiglass plate. A wing with an airfoil profile as its cross-section might convey a different fountain effect flow characteristic worth investigating.

In regard to PIV experiments for flow field visualization, enclosing the testing area should be considered to ensure proper saturation of the seed particle feeding. This effort helps for visualizing the region of interest while also avoiding flow interference around the rotors. When PIV is involved as a major part of future research, dedicating more effort to studying the flow interactions between the enclosing structure and rotor/wing configuration model would be beneficial to facilitate flow image capture and ultimately higher resolution of visualization.

Bibliography

[1] M. D. Maisel, D. J. Giulianetti and D. C. Dugan, The History of The XV-15 Tilt Rotor Research Aircraft From Concept to Flight, Washingdon D.C.: National Aeronautics and Space Administration, 2000.

[2] B. Burrage, "Studies of a Gunship Escort concept for the MV-22," in *International Powered Lift Conference*, Philadelphia, 2010.

[3] R. R. Prouty, "Which Do You Tilt: Wing Or Rotor?," in *Helicopter Aerodynamics*, Potomac, Phillips Business Information, 1985, p. 474.

[4] Y. Gibbs, "NASA Dryden Research Center Image Archive," 2 August 2010. [Online]. Available: https://www.nasa.gov/centers/dryden/multimedia/imagegallery/XV-15/EC81-15431.html. [Accessed 15 12 2016].

[5] Bell Boeing, V-22 Osprey, Seattle: Bell Boeing, 2010.

[6] F. F. Felker and J. S. Light, "Rotor/Wing Aerodynamic Interactions in Hover," in *42nd Annual Forum of The American Helicopter Society*, Washington D.C., 1986.

[7] M. A. McVeigh, "The V-22 Tilt-Rotor Large-Scale Rotor Performance/Wing Download Test and Comparison with Theory," in *11th European Rotorcraft Forum*, London, 1985.

[8] W. J. McCroskey, P. Spalart, G. H. Laub, M. D. Maisel and B. Maskew, "Airloads on Bluff Bodies, with Application to The Rotor-Induced Downloads on Tilt-Rotor Aircraft," National Aeronautics and Space Agency Ames Research Center, Moffett Field, 1983.

[9] W. Johnson, "Vertical Drag and Download," in *Rotorcraft Aeromechanics*, New York, Cambridge University Press, 2013, p. 118.

[10] N. Komerath and C. Matos, "Flowfield Issues Related to Tiltrotors," in *American Helicopter Society Tiltrotor/Runway Independent Aircraft Technology and Applications Specialists' Meeting*, Arlington, 2001.

[11] F. F. Felker, J. S. Light and R. E. Faye, "Reduction of Tilt Rotor Download Using Circulation Control," National Aeronautics and Space Agency Ames Research Center, Moffett Field, 1987.

[12] W. Johnson, "Calculation of Tilt Rotor Aeroacoustic Model (TRAM DNW) Performance, Airloads, and Structural Loads," in *American Helicopter Society Aeromechanics Specialists' Meeting*, Atlanta, 2000.

[13] M. A. Potsdam and M. J. Silva, "Tilt Rotor Aeromechanics Phenomena in Low Speed Flight," in *HPCMP Users Group Conference, DoD*, Williamsburg, 2004.

[14] S. W. Choi, M. K. Lee, S. Chang and J. M. Kim, "Development of Practical Tiltrotor UAV," in *50th American Institute of Aeronautics and Astronautics Aerospace Sciences Meeting*, Nashville, 2012.

[15] W. Johnson, Helicopter Theory, Princeton: Princeton University Press, 1980.

[16] R. G. Rajagopalan and C. K. Lim, "Laminar Flow of A Rotor in Hover," *American Helicopter Society*, vol. 36, no. 1, pp. 12-23, 1991.

[17] Banggood, *Walkera 4F200lm Model Helicopter*, Guangzhou: Banggood, 2013.

[18] Moon Hobby, *Walkera 4f200lm Swash Plate*, Shanghai: Moon Hobby, 2013.

[19] R. Gupta and P. J. Ansell, "Open-Loop and Closed-Loop Trailing-Edge Separation," in *54th AIAA Aerospace Sciences Meeting*, San Diego, 2016.

[20] Sukra Helitek, *Rotor Unstructured Solver Application (RotCFD) Theory*, Ames: Sukra Helitek, 2014.

[21] S. B. Pope, "An Introduction to Modelling and Simulation," in *Turbulent Flows*, New York, Cambridge University Press, 2000, pp. 336-343.

[22] N. J. Georgiadis, D. P. Rizzetta and C. Fureby, "Large_Eddy Simulation: Current Capabilities, Recommended Practices, and Future Research," NASA Glenn Research Center, Cleveland, 2009.

[23] J. M. McDonough, Introductory Lectures on Turbulence: Physics, Mathematics and Modeling, Lexington: University of Kentucky Department of Mechanical Engineering and Mathematics, 2007.

[24] N. Gourdain, F. Sicot, F. Duchaine and L. Gicquel, "Large Eddy Simulation of Flows in Industrial Compressors: A Path from 2015 to 2035," *Philosophical Transactions of The Royal Society*, vol. 372, no. 2022, 2014.

[25] Sukra Helitek, *Introduction to RotCFD: An Integrated Development Environment for Rotorcraft*, Ames: Sukra Helitek, 2015.

[26] W. J. F. Koning, "Wind Tunnel Interference Effects on Tiltrotor Testing Using Computational Fluid Dynamics," National Aeronautics and Space Agency Ames Research Center, Moffett Field, 2016.

[27] R. G. Rajagopalan, V. Baskaran, A. Hollingworth, A. Lestari, D. Garrick, E. Solis and T. Hagerty, "RotCFD - A Tool for Aerodynamic Interference of Rotors: Validation and Capabilities," in *American Helicopter Society Future Vertical Lieft Aircraft Design Conference*, San Francisco, 2012.

[28] J. W. Hong, "Hover and Cruise Flight Simulation of XV-15 Experimental Aircraft Using RotCFD," NASA Ames Research Center Aeromechanics Branch, Moffett Field, 2015.

[29] US Department of Transportation, Federal Aviation Administration, "Aerodynamics of Flight," in *Rotorcraft Flying Handbook*, Washington DC, Federal Aviation Administration, 2000, pp. 3-5.

[30] I. Fejtek and L. Roberts, "Navier-Stokes Computation of Wing/Rotor Interaction for a Tilt Rotor in Hover," *American Institute of Aeronautics and Astronautics*, vol. 30, no. 11, pp. 2595-2603, 1992.

[31] J. D. Singleton and W. T. Yeager, Jr., "Important Scaling Parameters for Testing Model-Scale Helicopter Rotors," *American Institute of Aeronautics and Astronautics Journal of Aircraft*, vol. 37, no. 3, pp. 396-402, 2000.

[32] A. J. Wadcock, G. K. Yamauchi, J. T. Heineck, M. J. Silva and K. R. Long, "PIV Measurements of the Wake of a Tandem-Rotor Helicopter in Proximity to a Ship," in *American Helicopter Society 4th Decennial Specialist's Conference*, San Francisco, 2004.

[33] O. Ahn, J. M. Kim and C. H. Lim, "Smart UAV Research Program Status Update: Achievement of Tilt-Rotor Technology Development And Vision Ahead," in *27th International Congress of The Aeronautical Sciences*, Nice, 2010.

[34] E. L. Hathaway, "Active and Passive Techniques for Tiltrotor Aeroelastic Stability Augmentation," The Pennsylvania State Unviersity College of Engineering Graduate School, University Park, 2005.

[35] M. J. Silva, G. K. Yamauchi, A. J. Wadcock and K. R. Long, "Wind Tunnel Investigation of The Aerodynamic Interactions Between Helicopters and Tiltrotors in a Shipboard Environment," in *American Helicopter Society 4th Devennial Specialist's Conference on Aeromechanics*, San Francisco, 2004.

[36] R. L. Peterson and T. H. Maier, "An Experimental Evaluation of Wind Tunnel Wall Correction methods for Helicopter Performance," in *American Helicopter Society 52nd Annual Forum*, Washington D.C., 1996.

[37] E. Romander, M. Betzina, M. Silva, A. Wadcock and G. Yamauchi, "Investigating Tiltrotor Formation Flight Via 1/48-Scale Wind Tunnel Experiment," in *American Helicopter Society 62nd Annual Forum*, Phoenix, 2006.

[38] W. Johnson, "Influence of Wake Models on Calculated Tiltrotor Aerodynamics," in *American Helicopter Society Aerodynamics, Acoustics, and Test and Evaluation Technical Specialists Meeting*, San Francisco, 2002.

[39] Sukra Helitek, Inc., "AirFoilTableGenerator(AFTGen) Application User Manual," Sukra Helitek, Ames, 2014.

[40] M. Potsdam and R. C. Strawn, "CFD Simulations of Tiltrotor Configurations in Hover," in *American Helicopter Society 58th Annual Forum*, Montreal, 2002.

[41] S. W. Choi, Y. Kang, S. Chang, S. Koo and J. M. Kim, "Development and Conversion Flight Test of a Small Tiltrotor Unmanned Aerial Vehicle," *American Institute of Aeronautics and Astronautics Journal of Aircraft*, vol. 47, no. 2, pp. 730-732, 2010.

[42] J. T. Heineck, G. K. Yamauchi, A. J. Wadcock, L. Lourenco and A. I. Abrego, "Application of Three-Component PIV to a Hovering Rotor Wake," in *American Helicopter Society 56th Annual Forum*, Virginia Beach, 2000.

[43] D. A. Conner and J. B. Wellman, "Hover Acoustic Characteristics of the XV-15 with Advanced Technology Blades," *American Institute of Aeronautics and Astronautics Journal of Aircraft*, vol. 31, no. 4, pp. 737-744, 1994.

[44] C.-Y. Xu, L.-W. Chen and X.-Y. Lu, "Large-Eddy Simulation of The Compressible Flow Past a Wavy Cylinder," *Journal of Fluid Mechanics*, vol. 665, pp. 238-273, 2010.

[45] H. Yeo and W. Johnson, "Performance and Design Investigation of Heavy Lift Tilt-Rotor with Aerodynamic Interference Effects," *American Institute of Aeronautics and Astronautics Journal of Aircraft*, vol. 46, no. 4, pp. 1231-1239, 2009.

[46] B. Mettler, C. Dever and E. Feron, "Scaling Effects and Dynamic Characteristics of Miniature Rotorcraft," *American Institute of Aeronautics and Astronautics Journal of Guidance, Control, and Dynamics*, vol. 27, no. 3, pp. 466-478, 2004.

[47] M. Raffel, H. Richard, K. Ehrenfried, B. Van der Wall, C. Burley, P. Beaumier, K. McAlister and K. Pengel, "Recording and Evaluation Methods of PIV Investigations on a Helicopter Rotor Model," *Experiments in Fluids*, vol. 36, pp. 146-156, 2004.

[48] H. Richard, J. Bosbach, A. Henning, M. Raffel, C. Willert and B. G. Van der Wall, "2C and 3C PIV Measurements on a Rotor in Hover Condition," in *13th International Symposium on Applications of Laser Techniques to Fluid Mechanics*, Lisbon, 2006.

[49] C. Barla, D. Favier, C. Rondot, C. Maresca, M. Raffel, H. Richard, J. Bosbach and H. Henning, "PIV Measurements of the Vortical Wake Behind Tilt-Rotor Blades," in *13th International Symposium on Applications of Laser Techniques to Fluid Mechanics*, Lisbon, 2006.

[50] A. Swanson and J. S. Light, "Shadowgraph Flow Visualization of Isolated Tiltrotor and Rotor/Wing Wakes," in *American Helicopter Society 48th Annual Forum*, Washington D.C., 1992.

[51] C. D. Coffen, "Tilt Rotor Hover Aeroacoustics," National Aeronautics and Space Agency Ames Research Center, Moffett Field, 1992.

[52] R. L. Meakin, "Moving Body Overset Grid Methods for Complete Aircraft Tiltrotor Simulations," in *American Institute of Aeronautics and Astronautics 11th Computational Fluid Dynamics Conference*, Orlando, 1993.

[53] M. Raffel, U. Seelhorst and C. Willert, "Vortical Flow Structures at a Helicopter Rotor Model Measured by LDV and PIV," in *22nd European Rotorcraft Forum*, Brighton, 1998.

[54] T. Poinsot, D. Veynante, F. Nicoud, B. Cuenot, L. Selle, G. Lartigue, L. Gicquel, V. Moureau and S. Candel, "Simulation Tools for 3D Reacting Flows," Princeton University Combustion Energy Frontier Research Group, Princeton, 2013.